Geomorphology 453 (2024) 109112

Contents lists available at ScienceDirect

Geomorphology

journal homepage: www.journals.elsevier.com/geomorphology

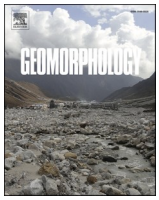

Spatiotemporal variations in frost cracking measures in two dimensions: A case study for rock walls in Jotunheimen, southern Norway

Justyna Czekirda [a,*], Alan W. Rempel [b], Bernd Etzelmüller [a], Sebastian Westermann [a]

[a] Department of Geosciences, University of Oslo, 0316 Oslo, Norway
[b] Department of Earth Sciences, University of Oregon, Eugene, OR 97403, USA

ARTICLE INFO

Keywords:
Rock walls
Frost weathering
Permafrost
Periglacial weathering
Frost crack modeling

ABSTRACT

The ground thermal regime has a profound impact on geomorphological processes and has been suggested to be particularly important for weathering processes in periglacial environments. Several frost-related damage indices have hitherto been developed to link climate and frost weathering potential in bedrock, although only for individual points or grid cells. Here, we model ground temperature and frost weathering potential in steep rock walls in the Jotunheimen Mountains, southern Norway, along a two-dimensional profile line for the Younger Dryas Stadial-Preboreal transition (c. 11.5 ka), the Holocene Thermal Maximum (c. 7.5 ka), the Little Ice Age (1750), and the 2010s. We use an established heat flow model and frost-cracking index based on the ice segregation theory. A central innovation of our model treatment is the implementation of ensemble simulations using distributions of automatically mapped crack radii in a rock wall, whereas previous frost damage models considered only a single characteristic crack radius. Our results allowed for the identification of sites with enhanced frost weathering. Such sites are typically found between rock walls and retreating glaciers, as well as in areas where snow depth changes abruptly, resulting in large thermal gradients. Hence, frost weathering may be highly active during glacier retreat, enhancing the damage to rock walls during deglaciation by adding to the damage from stress release. The coldest climates of the Younger Dryas Stadial-Preboreal transition and the Little Ice Age were generally most favorable for frost cracking. Such timing compares well with the knowledge about the timing of rockfall accumulations in Norway.

1. Introduction

Frost action dominates geomorphological processes in periglacial environments (e.g. Ballantyne, 2018). Although the efficiency of frost weathering and thus the periglacial imprint for long-term and large-scale landscape evolution have been questioned by recent research (André, 2003; French, 2016), geomorphological processes in cold, unglaciated areas are believed to be conditioned by seasonal and perennial ground ice despite the operation of azonal processes (Berthling and Etzelmüller, 2011). Recently, Egholm et al. (2015) explained the existence of high-elevation, low-relief surfaces, e.g. in southern Norway, by large-scale periglacial landscape evolution, the so-called "periglacial buzzsaw", over several million years through a combination of frost cracking and diffusive frost creep. Backwearing in cirques is thought to be a particularly effective mode of landscape smoothing (Oskin and Burbank, 2005; Steer et al., 2012), where denudation is likely driven by a combination of glacial and periglacial processes.

Rock wall retreat is a component of long-term landscape evolution in periglacial landscapes and exemplifies detachment-limited erosion, which mainly depends on the shear strength and weathering-susceptibility of rock instead of transport capacity. Compressional tectonics generates major flaws and joints in bedrock. Glacial debuttressing in recently glaciated areas may also lead to fracture formation (Ballantyne, 2002). Subsequently, pre-existing fractures are widened or new fractures are generated by chemical or physical weathering, such as thermal cracking due to thermal expansion stresses and weathering due to frost action. These processes further increase material detachability from rock faces, ultimately leading to gravity-driven material transport, especially when bedrock permafrost thaws (Krautblatter et al., 2013; Murton et al., 2006). Rock wall permafrost is exceptionally vulnerable due to its rapid thermal response to atmospheric warming, exacerbated by low ice contents, three-dimensional effects, and shallow snow cover (Boeckli et al., 2012; Gruber and Haeberli, 2007; Myhra et al., 2017; Noetzli et al., 2007). The occurrence of rock falls induced by thawing

* Corresponding author.
E-mail address: justyna.czekirda@geo.uio.no (J. Czekirda).

https://doi.org/10.1016/j.geomorph.2024.109112
Received 11 April 2023; Received in revised form 16 February 2024; Accepted 21 February 2024
Available online 23 February 2024

permafrost has increased in the European Alps since the end of the last century (Fischer et al., 2012; Ravanel and Deline, 2011), particularly during unusually hot summers (Gruber et al., 2004).

Traditionally, the drivers for frost weathering were mainly related to freeze-thaw cycles and the 9 % volumetric expansion of water when it freezes to ice in situ, so-called "freeze-thaw weathering" (e.g. McGreevy and Whalley, 1982). Such a process requires a closed system and saturated conditions, with most damage expected to occur very close to 0 °C; damage at lower temperatures in undersaturated conditions while fluid migration pathways are present requires a different mechanism. Accordingly, some studies have considered volumetric expansion as a frost weathering process that may be effective close to the surfaces of saturated rocks subject to rapid freezing, particularly in water-filled joints, or in rocks with small specific surface areas (e.g. Matsuoka, 1990; Matsuoka and Murton, 2008). Other studies have argued against the importance of "freeze-thaw weathering" due to volumetric expansion in nature (e.g. Hallet et al., 1991) and instead invoke segregated ice growth as a much more effective and pervasive frost-damage mechanism. Ice segregation in rocks refers to ice growth due to water migration (i.e. "cryosuction"), induced by chemical-potential gradients, towards the freezing front. This is the same mechanism responsible for frost heave in fine-grained soils. In the "ice-lensing model" of Walder and Hallet (1985), frost-induced rock damage results from the temperature-dependent buildup of ice pressure inside slowly growing cracks. Their results showed that frost cracking is most effective at ground temperatures between approximately −15 and − 4 °C, with the exact temperature range depending on initial crack size and the hydraulic- and fracture-mechanical properties of bedrock. At higher temperatures, ice pressure and thus the stress-intensity factor are too low for crack growth, whereas at lower temperatures, the low hydraulic conductivity of partially ice-clogged fluid pathways inhibits the water supply needed for crack growth. Walder and Hallet (1985) emphasized that freeze–thaw oscillations are not required for effective frost weathering and instead the main limiting factor for crack growth is water transport, although freeze–thaw cycles may often help to enhance water supply (Walder and Hallet, 1986). This theoretical model for ice-induced crack growth was later tested by measuring microfracture activity in the laboratory for sandstone specimens subject to freezing, with results confirming that most frost damage occurred in a frost-cracking window (FCW), which fell between −6 and − 3 °C (Hallet et al., 1991). Laboratory experiments by Murton et al. (2006) using wet chalk specimens showed that: (1) frost damage was associated with ice segregation during thawing cycles, and not freezing cycles themselves, (2) fractures caused by frost weathering were parallel to the cooling surfaces, (3) ice lenses were formed, and (4) the depth of fractures depended on whether they resulted from bi- or unidirectional freezing. Duca et al. (2014) conducted the first laboratory study using hard, intact rock specimens of gneiss and showed that ice segregation also operates in harder rock types, although the microcracking they observed occurred between −2.7 and − 0.5 °C, which is a higher temperature range than previous studies (e.g. Matsuoka and Murton, 2008) would have predicted for such hard rocks.

Tracking the growth of each crack within a landscape would be a daunting task, and instead efforts to gauge the contribution of frost damage to landscape evolution have motivated the development of several one-dimensional frost-cracking indices that attempt to link key climate attributes with frost-cracking potential due to ice segregation in rocks. Anderson (1998) implemented the first frost-cracking index, which accounts for a correlation between frost damage and the time spent within an assumed FCW. Hales and Roering (2007) based their frost-weathering index on the premise that, in addition to time spent within the FCW, the temperature gradient is important for controlling the chemical potential gradients that facilitate water transport during frost cracking. Anderson et al. (2013) extended the latter model with a penalty function to address limits on water availability that increase with the distance between unfrozen reservoirs and potential frost-cracking sites. Lastly, in Rempel et al. (2016) a temperature-dependent hydraulic conductivity was introduced, with frost damage assumed to correlate with the porosity changes that accompany gradients in water flux when the temperature is low enough for ice growth to extend cracks.

The mentioned frost cracking indices assume that heat flow occurs one-dimensionally, whereas various ground temperature modeling studies implement realistic three-dimensional heat flow inside steep mountains (Noetzli and Gruber, 2009; Noetzli et al., 2007). Different rock surface temperatures depending on the aspect of rock faces have been measured in southern Norway (Czekirda et al., 2023; Hipp et al., 2014; Magnin et al., 2019), certainly influencing ground temperature distribution and thus frost weathering processes. To our knowledge, only a few studies explicitly mention such lateral effects as important in their study areas. Studies of coastal cliff temperatures in Svalbard related the large frost weathering potential in the area to thermal gradients due to snow cover variations (Ødegård and Sollid, 1993; Ødegård et al., 1995). Farbrot et al. (2007) calculated relatively high retreat rates (0.4–0.6 mm a^{-1}) in rock walls above talus-derived rock glaciers in the Tröllaskagi Peninsula in northern Iceland, which were attributed to large thermal gradients between the isothermal snowpack arising from maritime climate and colder permafrost-underlain rock walls. In addition, the study by Myhra et al. (2019) showed large thermal gradients between shaded rock walls and talus slopes, implying that such boundary areas may be important spots for frost weathering.

We hypothesize that lateral effects are important for frost weathering processes in rock walls. This study aims to increase knowledge about the importance of the lateral effects on frost weathering processes in rock walls, exemplified by those situated in the alpine periglacial environment of the Jotunheimen Mountains in southern Norway. The following research objectives are set: (1) extend the existing one-dimensional frost-weathering index proposed by Rempel et al. (2016), described in more detail in Section 3.1, to two-dimensional configurations; (2) model ground temperature in two dimensions (Section 3.2); (3) run the frost damage model based on the modeled subsurface thermal fields (Section 3.3); and (4) evaluate the spatiotemporal patterns of frost weathering. In contrast to previous studies (Rempel et al., 2016; Walder and Hallet, 1985) that are formulated in terms of a single characteristic/initial crack size, we account for the population of initial crack radii in a rock wall by using ensemble-based modeling.

2. Site description

We focus on two rock walls below the Veslpiggen (or Vesle Galdhøpiggen) Plateau, located in the Galdhøpiggen massif, western Jotunheimen, central southern Norway (Fig. 1). The Galdhøpiggen massif is one of the highest mountain areas in Norway. The study area is within the tectonic unit of the Jotun-Valdres Nappe Complex with high-grade intrusive rocks. The bedrock in the area is composed of pyroxene granulite with a composition from gabbroic to quartz mangeritic (Lutro and Tveten, 2012). Rock walls below the Veslpiggen Plateau probably formed as a result of the cumulative operation of various geomorphological processes during the multiple local glaciations and non-glacial periods throughout the Quaternary, similar to other larger-scale erosional bedrock landforms in Norway (Fredin et al., 2013). The most important geomorphological processes in those rock walls have probably been glacial and periglacial erosion, possibly with some contribution from debuttressing effects. These processes were probably not effective during the full-scale Pleistocene glaciations because other studies suggest that these mostly cold-based ice sheets were non-erosive in Norway, except in the deep valleys and fjords (Kleman et al., 2008). Hughes et al. (2015) suggest a deglaciation onset in the study area around 12 ka (the Younger Dryas Stadial), a rapid ice retreat from 10 ka and completion of the ice-sheet glaciation around 9.5 ka (the Boreal period) when the local valley at an elevation of around 800 m was completely deglaciated. All glaciers in Norway melted away during the

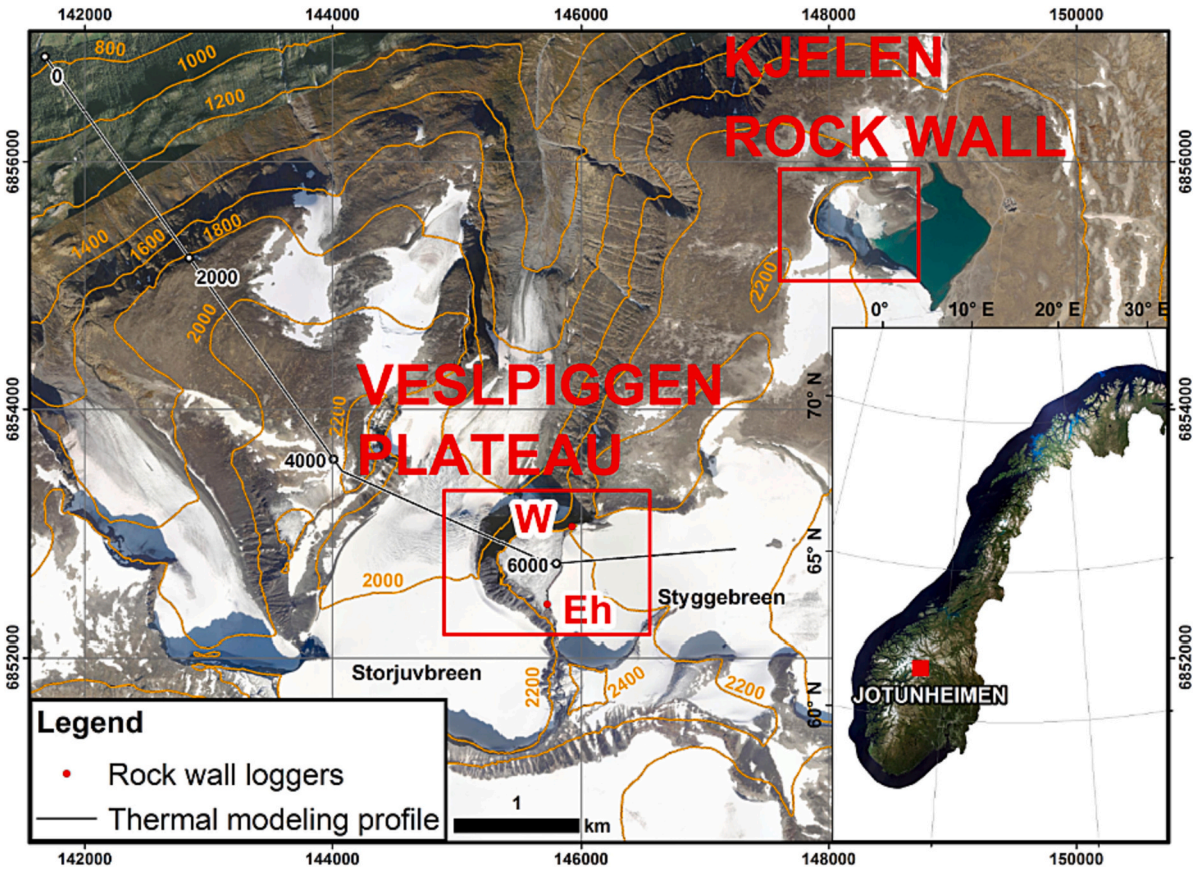

Fig. 1. The Veslpiggen modeling profile. Red points show the location of rock wall loggers in the various expositions: Eh – east-facing logger at a higher elevation, W – west-facing logger. Numbers along the modeling profile indicate distance in meters. Map background courtesy of © Statens kartverk, Geovekst og kommunene. UTM zone 33 N.

relatively warm period of the Holocene Thermal Maximum, although the timing of the disappearance varies (Nesje et al., 2008). Glaciers reformed during the Neoglaciation that in Norway began around 6–5 ka. The maximum Holocene glacier extent was reached during the Little Ice Age period, which culminated around 1750 in Norway. There has been extensive permafrost research in the gentle terrain of the nearby Juvflye area. Several boreholes have been drilled in the area (Farbrot et al., 2011; Ødegård et al., 1992), including a deep PACE borehole (129 m) in the continuous permafrost zone at 1894 m elevation (Harris et al., 2001). At the highest elevations (above ~1850 m) permafrost has likely been present throughout the entire Holocene (Lilleøren et al., 2012). Magnin et al. (2019)'s statistical model results suggest that the lower limit of rock wall permafrost in the Jotunheimen area is at approximately 1550 and 1150 m elevation for south- and north-facing rock walls, respectively.

The two rock walls along the two-dimensional model profile (Fig. 1) have easterly (elevation of 2280–2300 m) and westerly aspects (elevation of 2150–2190 m). The Veslpiggen Plateau is covered by blockfields and underlain by continuous permafrost, as confirmed by ground temperature modeling (Czekirda et al., 2023). The east-facing flank of the plateau is at present covered by the Styggebreen Glacier (Fig. 1) up to an elevation of 2275 m, which influences the ground thermal regime within the rock wall (Czekirda et al., 2023). The rock walls in the study area are monitored by shallow (10 cm depth) temperature loggers (Fig. 1) (Magnin et al., 2019), which allowed for calibration and estimation of ground surface temperature (GST). Our estimated mean annual ground surface temperature (MAGST) for the east-facing rock wall is −1.3 °C (2300 m) for the 2010s with an annual amplitude of 12.1 °C. MAGST is lower at the lower west-facing rock wall and is estimated at −3.3 °C (2180 m) for the 2010s with an annual amplitude of 9.3 °C. The blockfields on the plateau are likely colder and have estimated MAGST of −4.2 °C (2320 m; the 2010s) and a smaller annual amplitude of 5.4 °C due to the insulating effect of snow cover and lower amount of incoming shortwave solar radiation.

3. Methods and data

3.1. 2D frost damage model

Intermolecular interactions cause liquid water to wet both ice and rock/soil surfaces so that "premelted" liquid can persist in porous geological materials even when the temperature is several degrees below the normal bulk melting temperature of $T_m = 273.15$ K (Dash et al., 2006). This behavior is crucial to models of ice segregation, both because the premelted liquid forms connected pathways that can supply ice growth and allow the frozen mass to often exceed the initial moisture capacity of the unfrozen rock, and because the intermolecular interactions responsible for premelting produce a net thermomolecular pressure that increases as the temperature T is reduced, enabling the propagation of cracks at temperatures well below T_m. The dynamics of ice segregation can be formulated in terms of standard conservation laws. Differences between the thermomolecular pressure and the stresses that resist the expansion of segregated ice set the distribution of liquid pressures, leading to liquid pressure gradients that commonly run parallel to temperature gradients (Dash et al., 2006; Rempel et al., 2016); liquid water migration to the solidification front follows as a direct consequence. Frost damage associated with crack growth becomes possible at temperatures that are sufficiently low, or equivalently at undercoolings $\Delta T = T_m - T$ that are sufficiently high, for the thermomolecular pressure exerted by the ice on the rock matrix to promote

the stress concentrations at crack tips that are necessary to propagate fractures (Rempel et al., 2016; Walder and Hallet, 1985). However, as the temperature drops, ice formation also causes the hydraulic conductivity in the frozen rock matrix to drop substantially, so that the water flux parallel to the temperature gradients must decrease as well (Rempel et al., 2016).

The key assumption of Rempel et al. (2016)'s model is that frost weathering potential is correlated with ice growth at sufficient undercoolings for the thermomolecular pressure to propagate fractures. Accepting this premise, mass balance considerations then imply that the spatiotemporal porosity changes that must result from gradients in the liquid water supply to growing segregated ice can be interpreted as a measure of frost weathering potential. It should be noted, however, that some ice expansion can be accommodated elastically, and is hence reversible, so modeled porosity changes do not necessarily gauge frost damage directly and resulting predictions should thus be interpreted as a qualitative measure of damage. In this work, the following assumptions from the original model are retained (Rempel et al., 2016):

1) Frost damage can occur only when the net thermomolecular pressure against the rock matrix is greater than a critical cracking pressure P_c, which dictates the upper-temperature limit for frost cracking ΔT_c. We term ΔT_c as the "undercooling for frost cracking", i.e. the absolute temperature difference between T_m and the upper-temperature threshold for the onset of frost-induced porosity increase. Following linear elastic fracture mechanics, we expect P_c to depend on the mode I (tensile) fracture toughness through "the critical stress-intensity factor" K_{IC}, and the crack radius c, so that

$$\Delta T_c \approx \frac{T_m}{\rho L} P_c \approx \frac{T_m}{\rho L} \frac{\sqrt{\pi}}{2} \frac{K_{IC}}{\sqrt{c}}, \tag{1}$$

where ρ is the ice density (920 kg m^{-3}), and L is the specific latent heat of fusion (334 kJ kg^{-1}).

2) The generalized Clapeyron equation approximates the undercooling ΔT as proportional to the difference ΔP between ice pressure against the crack walls and the lower liquid pressure in water films that enables liquid water supply. Thus, the model assumes that liquid water must be available when ice is present.
3) Liquid water flow is redistributed according to Darcy's law with a temperature-dependent permeability $k(T)$ that is parametrized using the power-law function

$$k(T) = k_c \left(\frac{\Delta T_c}{\Delta T} \right)^{\alpha}, \tag{2}$$

where α is the unitless power-law exponent (here 4), and k_c denotes the permeability at ΔT_c, typically between 10^{-24} and 10^{-16} m^2. Eq. (2) implies that k decreases dramatically as temperature drops and ice formation inhibits water movement. This assumption justifies the lack of an explicit lower temperature limit for frost cracking in the model, i.e. the equivalent of the lower temperature threshold in FCW. The unfrozen hydraulic permeability k_0 can be used to estimate k_c as

$$k_c \equiv k_0 \left(\frac{\Delta T_f}{\Delta T_c} \right)^{\alpha} \tag{3}$$

where ΔT_f – the undercooling for ice formation – is set to 0.1 °C to obtain the results described below.

4) Saturated conditions are idealized as always prevailing in rock pores (Rempel et al., 2016).

In Rempel et al. (2016), the model described above is applied in one dimension. We derived a two-dimensional version of the model by using the same underlying equations (see Appendix A. Frost damage model derivation) that satisfy the mass balance constraint. We compute spatiotemporal porosity changes Δn in two dimensions for each node with Cartesian coordinates x and y at time t:

$$\Delta n(x,y,t) = \frac{D\Delta T_c^{\alpha-1}}{\alpha} \int_{t_c}^{t} \Delta T(x,y,t)^{-\alpha} \left[\frac{\alpha}{\Delta T(x,y,t)} \left(\nabla T(x,y,t) \right)^2 + \nabla^2 T(x,y,t) \right] dt \tag{4}$$

where the symbols denote: D – the frost weathering diffusivity, ∇T – the temperature gradient [°C m^{-1}] and $\nabla^2 T$ – the Laplacian [°C m^{-2}]. Here, D is defined as:

$$D = \frac{\rho L}{T_m \mu} \alpha k_c \Delta T_c \tag{5}$$

where μ denotes the dynamic viscosity of water (1.8 mPa s). The accumulated porosity change for one year is defined as:

$$\Delta n(x,y) = \frac{D\Delta T_c^{\alpha-1}}{\alpha} \int_{\Delta T > \Delta T_c, 1\ year} \Delta T(x,y)^{-\alpha} \left[\frac{\alpha}{\Delta T(x,y)} \left(\nabla T(x,y) \right)^2 + \nabla^2 T(x,y) \right] dt. \tag{6}$$

The integration limits allow us to only track the frost-induced porosity change for days when the ground temperature at a given node is below the threshold value of $-\Delta T_c$. The implied frost damage is thus a function of: (1) rock strength parameters through ΔT_c that dictates when frost cracking starts (Eq. (1)), (2) D that determines the rock susceptibility to frost damage (Eq. (5)), (3) ground temperature, and (4) α that shapes the hydraulic permeability decline with decreases in ground temperature. The second term in Eq. (6) has a minor influence on porosity changes, and its contribution is exactly zero in idealized cases where the annual temperature forcing is periodic and sensible heat changes dominate (Carslaw and Jaeger, 1959). In this study, we account for latent heat effects and therefore we keep the second term, although its influence remains minor, because most freezing takes place at higher temperatures and sensible heat changes tend to be more important than latent heat effects in the temperature range where frost cracking occurs.

3.2. Ground temperature modeling

We run the CryoGrid 2D heat conduction model with the effects of latent heat (Myhra et al., 2017) for four time slices (10-year periods) around: (1) the Younger Dryas-Preboreal transition (YD/PB, c. 11.5 ka), (2) the Holocene Thermal Maximum (HTM, c. 7.5 ka), (3) the Little Ice Age (LIA, 1750), and (4) the 2010s.

Simulations for the 2010s: We mostly use the methods for ground temperature modeling presented in Czekirda et al. (2023). The ground thermal modeling in the latter study was based on runs with monthly time steps forced by the regional monthly data set provided by the Norwegian Meteorological Institute (Hanssen-Bauer et al., 2006) as well as meteorological station data or the seNorge observational gridded datasets (Lussana, 2020). In the previous simulations, the model was run at monthly time steps, which we consider insufficient for this study. Hence, we rerun the model using the output from the monthly time steps as the initial temperature for the daily runs. We run the model only for the 2010s. We adjust daily air temperature data from the seNorge datasets (Lussana, 2020) and/or data from meteorological stations if available, so the mean monthly air temperature in this study is the same as in Czekirda et al. (2023). This procedure minimizes the difference in comparison to previous runs and avoids the issues with lapse rate in the seNorge datasets. Other methods are the same as in Czekirda et al. (2023), where mesh, ground stratigraphy, meteorological data and other parameters are described in detail. We only use the main thermal scenario from the aforementioned study, where several thermal sensitivity simulations were run.

We created a 2D-model profile for the Jotunheimen site by drawing a transect across the mountain. Elevation at the upper boundary of the two-dimensional domain was extracted from a digital elevation model (Fig. 2A). Furthermore, we needed to define the stratigraphy of the model domain, and we used the surface deposits map with some refinements based on the orthophotos to specify the volumetric contents of the subsurface (Fig. 2B; Table 1).

***Simulations for the Younger Dryas, the Holocene Thermal Maximum and the Little Ice Age*:** As long-term air temperature, we use the TraCE-21 ka dataset (Liu et al., 2009), filled with NGRIP ice core data (NGRIP, 2004) for the HTM. Mean annual surface air temperature (SAT) was computed along the profile using the long-term air temperature datasets and the 2010s lapse rates. Subsequently, we compute monthly SATs using the 2010s air temperature amplitudes. Finally, GST, which the CryoGrid 2D requires as forcing, is estimated using slope gradient-dependent nF-factors to account for snow cover (Smith and Riseborough, 2002) and site- and aspect-specific monthly surface offsets to account for the incoming shortwave solar radiation in rock walls (Czekirda et al., 2023) (Fig. 2B). We run the first steady-state simulation for the permafrost model at the local deglaciation onset and assume a warm-based ice sheet with the basal temperature at the ice melting point (T_m). We derived the deglaciation dynamics for each site from the DATED-1 dataset, which contains time-slice maps of the Eurasian Ice Sheet margins for every one-thousand-year transition (Hughes et al., 2015). For each map, we computed ice thickness h for a distance x from the ice divide assuming a perfectly plastic parabolic ice sheet with radius

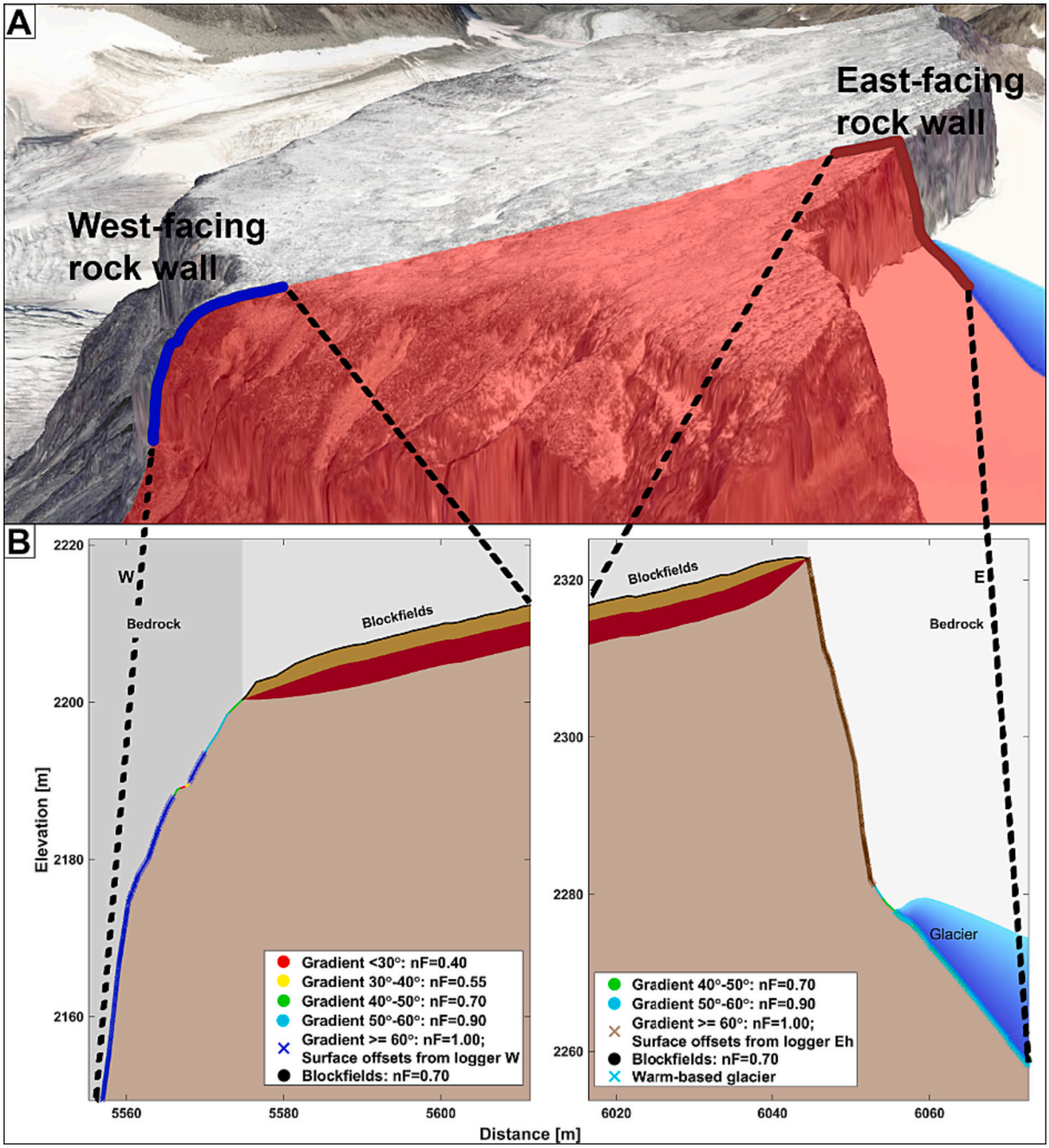

Fig. 2. **A**: The 2D-model profile (red transparent polygon) draped over surface topography. 2.5D background courtesy of: © Statens kartverk, Geovekst og kommunene. **B**: Model domain and forcing assumptions for surface nodes along the model profile. nF – freezing n-factor. The volumetric contents of the soil constituents for various subsurface layers are listed in Table 1.

Table 1
Assumed depths of subsurface layers, along with volumetric fractions of the soil constituents for each layer: θ_w – volumetric water content; θ_m – volumetric mineral content; θ_a – volumetric air content; z – depth. The row colors correspond to the subsurface colors depicted in Fig. 2B.

z [m]	θ_w [-]	θ_m [-]	θ_a [-]
Bedrock			
>0	0.05	0.95	0.00
Blockfields			
<2	0.10	0.60	0.30
2–5	0.40	0.60	0.00
>5	0.05	0.95	0.00

L (Paterson, 1994):

$$h = \left(\frac{2\tau_0}{\rho g}(L - x)\right)^{1/2} \quad (7)$$

where the basal shear stress τ_0=150 kPa (Vie, 2012) and g is the acceleration due to gravity. Subsequently, we interpolated the one-thousand-year ice thicknesses to yearly estimates. The onset of deglaciation for the highest peaks at the Veslpiggen Plateau occurred around 12 ka. We proceed with transient runs at yearly time steps until the YD/PB transition (11.5 ka), HTM (7.5 ka) and LIA (1750). During deglaciation, we use T_m for ice-covered parts along the profile and GST for unglaciated parts. We run the permafrost model at daily steps for 10 years at the mentioned end periods using the same SAT amplitudes as for the 2010s, accounting for the SAT offset between the 2010s and YD/PB, HTM or LIA. The derived offset is −4.7 °C between the YD/PB and 2010s, +1 °C between the HTM and 2010s and − 3 °C between the LIA and 2010s. The elevation of the Fennoscandian Ice Sheet at 11.5 ka is modeled at 2180 m. We remove glaciers in Jotunheimen in 9.5–8.5 ka and 7.5–6.5 ka according to the glacier variations in the Smørstabbtindan area (Matthews and Dresser, 2008; Nesje, 2009).

3.3. Frost damage modeling

***Mechanical and hydraulic properties of bedrock*:** We estimated K_{IC} from uniaxial compressive strength σ_C using an equation from Chang et al. (2002). The study site has orthopyroxene gneiss bedrock with an assumed σ_C between 90 and 225 MPa, based on the value for amphibiotic gneiss from Hanssen (1988). These yield estimated K_{IC} values between 1.44 and 2.01 MPa $m^{1/2}$. In our simulations, we choose a uniform mean value of 1.7 MPa $m^{1/2}$. Crystalline bedrock at the study site has low unfrozen permeability with an assumed uniform value of 5×10^{-17} m^2 (Nilsen and Thidemann, 1993).

Note that the frost damage model was formulated to account for homogenous crack radii as defined in Eq. (1) to set the upper temperature limit for frost damage. In reality, a population of cm-scale, mode I cracks is expected within a single rock wall, and hence a choice must be made for the characteristic crack radius c that is most relevant for the onset of significant frost weathering. In our study, rather than pick a single value for c we take advantage of the statistical distribution of crack radii that is approximated from the mapped crack lengths observed in a selected rock wall. To avoid manual digitalization of fracture traces, which is both time-consuming and somewhat associated with a subjective interpretation, we employed MATLAB-based software for ridge detection using the complex shearlet transform to automatically detect fractures based on an orthomosaic (Prabhakaran et al., 2019). We conducted fieldwork to collect drone imagery from the 260 m high Kjelen rock wall (See Fig. 1 for the location), created an ultra-high quality dense point cloud in the photogrammetric Agisoft Metashape software using this imagery (Fig. 3A), and subsequently exported a 10 × 10 m orthomosaic with 1 cm^2 resolution for a section where the drone was closest to the rock wall (Fig. 3B). Fig. 3B shows the mapped cracks and the algorithm gave satisfactory results for our rock wall section.

The histogram of the mapped crack radii is depicted in Fig. 4A. We fitted a log-normal probability density function (PDF) to the data (Fig. 4A), which yielded the parameters $\mu = 1.58$ and $\sigma = 0.76$, which are used in the statistical formulae included on Fig. 4A for crack dimensions measured in cm. Fig. 4B shows ΔT_c as a function of crack radius computed from Eq. (1) assuming fracture toughness $K_{IC} = 1.7$ MPa $m^{1/2}$. Fig. 4C shows the distribution of the ensemble sample with 500 random numbers from the fitted log-normal distribution.

***Computation of porosity changes*:** We implemented the frost damage model as presented in Section 3.1 and verified the implementation by comparing it with 1D runs shown by Rempel et al. (2016). We note that we do not aim at the application of the frost damage model in a transient way for longer periods, and present the results as annual means for the four time periods 11.5 ka (YD/PB), 7.5 ka (HTM), 1750 (LIA) and the 2010s. We accumulate porosity change in each vertex in the finite element mesh for each year in each time period using Eq. (6) and subsequently compute an annual mean for a 10-year period. We run the model for the population of crack radii that define ΔT_c shown in Fig. 4C. By performing the statistical runs, we assume that there is no interaction between various cracks and that each crack grows independently of others, i.e. each model run for various ΔT_c is run independently.

4. Results

4.1. Ground temperature modeling

The YD/PB was a cool period, and SAT was estimated to be −4.7 °C lower than in the 2010s (Fig. 5), and the modeled ground temperature in the rock walls is between −9 and − 5 °C. The HTM was a warmer period, with SAT estimated to be +1 °C higher than in the 2010s. The modeled rock wall temperature is between −4 and 0 °C for that period, which is even higher than over the 2010s when the modeled rock wall temperature is between −5 and − 1 °C. During the LIA, the modeled rock wall temperature is between −7 and − 4 °C. In general, the west-facing rock wall has lower modeled ground temperature than the east-facing rock wall, and its temperature is quite similar to the blockfields on the plateau, whereas the east-facing rock wall is up to 4 °C warmer than the blockfields on the adjacent plateau (Fig. 5). The difference in ground temperature between the east-facing and west-facing rock walls is around 1–3 °C. With the modeled thermal regime range for rock walls since deglaciation in mind, i.e. mean ground temperature range between −9 and 0 °C, we proceed with a description of the modeled porosity changes.

4.2. Frost damage modeling

We present the results of the porosity model for the YD/PB for two cases: (1) one in which ΔT_c is only computed for the median crack radius of 4.86 cm (Fig. 6A), (2) and one in which Δn is computed as a mean of the ensemble-based simulations for the sample of ΔT_c (Fig. 6B). Figs. 7 and 8 illustrate the same results for the remaining decennia. We also computed the average Δn with depth for various zones presented in Fig. 6: zones 1 and 6 include blockfields, zones 2 and 8 include moderately steep slopes, zones 3 and 7 include rock walls with various expositions, zones 4 and 9 include parts of rock walls that were or still are just at an elevation of an ice sheet or a glacier, zones 5 and 10 include previously or currently glaciated portions of the profile. The average profiles of porosity change Δn with depth in the various zones are shown in Fig. 9. Fig. 10 depicts average profiles of Δn with depth for zones with

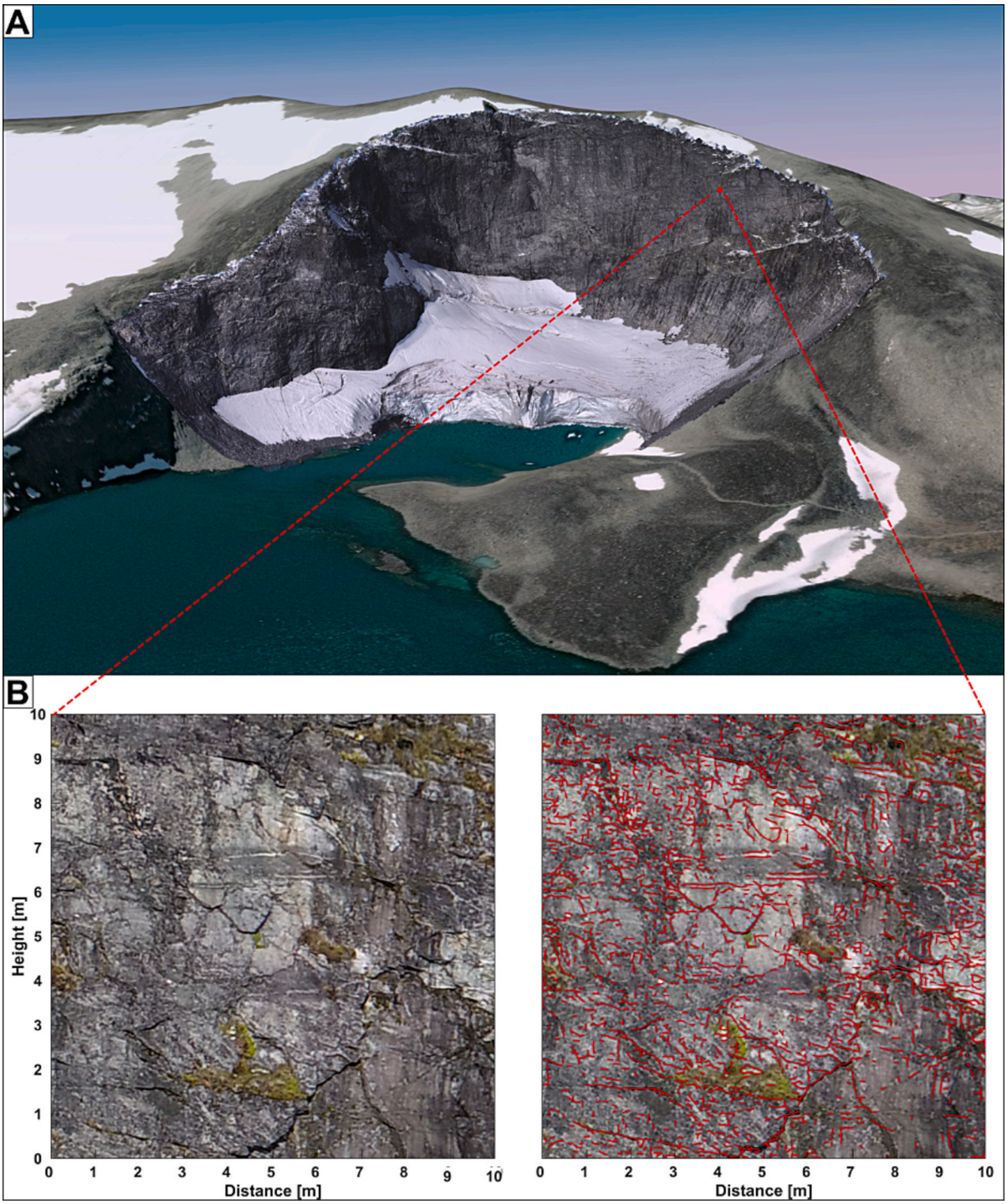

Fig. 3. **A**: Dense point cloud from the 260-m-high Kjelen rock wall (See Fig. 1 for the location), together with the location of the selected rock wall section (tiny red rectangle) draped over 2.5D background courtesy of © Mapbox, © OpenStreetMap, © Maxar. **B**: Orthomosaic (left image) and automatically mapped cracks (red lines) draped over the orthomosaic (right image).

rock walls.

ΔT_c is 6.1 °C for the median crack radius of 4.86 cm, meaning that frost-induced porosity increase only occurs for ground temperatures lower than −6.1 °C, i.e. the optimal thermal conditions for frost cracking require quite low ground temperatures. Hence, the results from the median crack radius simulations suggest that the frost cracking potential was greatest during the YD/PB period (Figs. 6A, 7, 9A). Over the HTM, frost cracking was least active due to the highest modeled ground temperatures, except in areas where we assumed that the present-day glacier was absent in that period. The modeled frost cracking potential for the LIA and 2010s falls between the large frost cracking potential in the YD/PB and the smallest frost cracking potential in the HTM, with the LIA frost damage slightly smaller than the YD/PB frost potential. Since ensemble simulations allow for frost cracking operating across wider climatic conditions, the computed Δn is always larger and reaches deeper than in the median crack radius simulations (Figs. 6B, 8, 9B). The evolution of frost cracking potential also shows that the temporal differences in Δn are much smaller in the ensemble simulations than in the

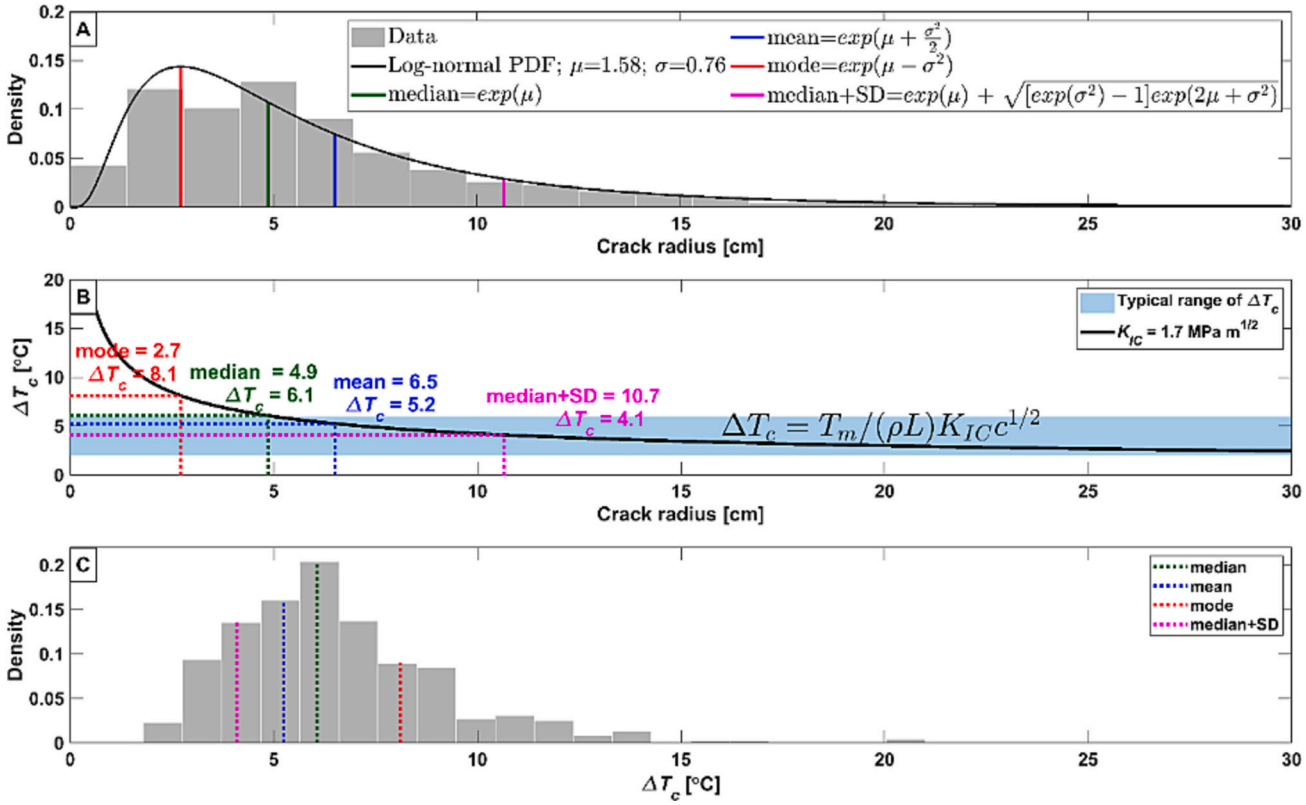

Fig. 4. **A:** Distribution of crack radii and a fitted log-normal probability density function (PDF) with parameters μ and σ. SD – standard deviation. **B**: Undercooling for frost cracking ΔT_c as a function of crack radius c for fracture toughness K_{IC}=1.7 MPa $m^{1/2}$. Physical constants in the equation are: T_m – the bulk melting temperature (273.15 K), ρ – the ice density (920 kg m^{-3}), L – the specific latent heat of fusion for water (334 kJ kg^{-1}). **C**: Distribution of undercooling for frost cracking ΔT_c sample used in the ensemble simulations.

median crack radius simulations (Fig. 9). In contrast to the median crack radius simulations, the YD/PB is not necessarily the period with the largest frost cracking potential according to the ensemble simulations, depending on the zone. The LIA period also has a large frost-cracking potential in the ensemble simulations. The HTM is usually the period with the smallest potential weathering in the rock walls, according to the ensemble simulations.

Ensemble simulations are averaged values from 500 simulations with various crack radii and we evaluated which crack radius is the most similar to average ensemble values (Fig. 10B). The results suggest that a crack radius of around 8 to 9 cm dominates the mean computed in the ensemble simulations. A crack radius of around 8 to 9 cm corresponds to ΔT_c between 4.5 and 4.7 °C and could be approximated by $median + a^*SD$, where coefficient a=0.55–0.7. It seems reasonable to assume that the median crack radius is the most important for frost damage potential; however, our results suggest otherwise, indicating that ΔT_c from the median crack radius simulations is 1.5 °C too high. Therefore, the median crack radius simulations show the biggest frost damage potential for colder climate conditions, whereas the ensemble simulations favor slightly warmer climate conditions for shaded rock walls and colder climate conditions for sun-exposed rock walls.

Our two-dimensional profiles show that frost damage always decreases with depth in an exponential way (Figs. 9 and 10). Our results do not reproduce spikes in frost damage potential at a particular depth, as shown in Rempel et al. (2016)'s study. We modeled a more rapid decrease with depth than shown for the one-dimensional profiles in Rempel et al. (2016). Two-dimensional temperature gradients are expected to have a sharper decrease with depth than 1D profiles due to the surface topography in our study.

We assumed in the ground temperature modeling that the snow distribution depends on the slope gradient and rock walls (slope gradient >60°) are snow-free. In addition, we added surface offsets arising from incoming shortwave solar radiation in the rock wall sections. Hence, along our profiles rock walls are the areas with the largest GST amplitudes, both in winter and summer. The amplitude of the MAGST is around 12 °C at the east-facing rock wall, around 9 °C at the west-facing rock wall and around 5 °C at the blockfield-covered plateau. For moderately steep slopes, we ignore surface offsets for the summer period. The assumptions from the ground temperature modeling influence the results and rock walls generally have the largest frost weathering potential along profiles, larger than blockfields and moderately steep slopes (Fig. 9). However, the east-facing moderately steep slopes may have larger frost cracking potential than the east-facing rock walls at certain depths, according to the median crack radius simulations. According to the ensemble simulations, the east-facing sun-exposed rock wall has the largest and deepest frost cracking potential, except for Zones 4 and 9.

Furthermore, the climate conditions do not seem to be a limiting factor for frost cracking in the uppermost 1 m of the subsurface, yielding very similar results for various periods and zones in the ensemble and median crack radius simulations (Figs. 9 and 10). The differences at depth seem to be more pronounced. Nevertheless, there are areas where frost cracking potential is much larger close to the surface than anywhere else, even in the uppermost 1 m, namely in Zones 4 and 9 (Figs. 9 and 10). All simulations show that critical points for frost cracking are concentrated in the vicinity of the melting ice sheet, the glacier and anywhere where we anticipate a sharp transition in snow conditions, resulting in large ground thermal gradients in these areas (the black areas in Figs. 6–8). The temperature at the glacier bed was assumed to be 0 °C; hence, the areas between the rock walls and the melting ice sheet on the west-facing rock wall (YD/PB) and the glacier on the east-facing rock wall (except HTM) have particularly large ground thermal

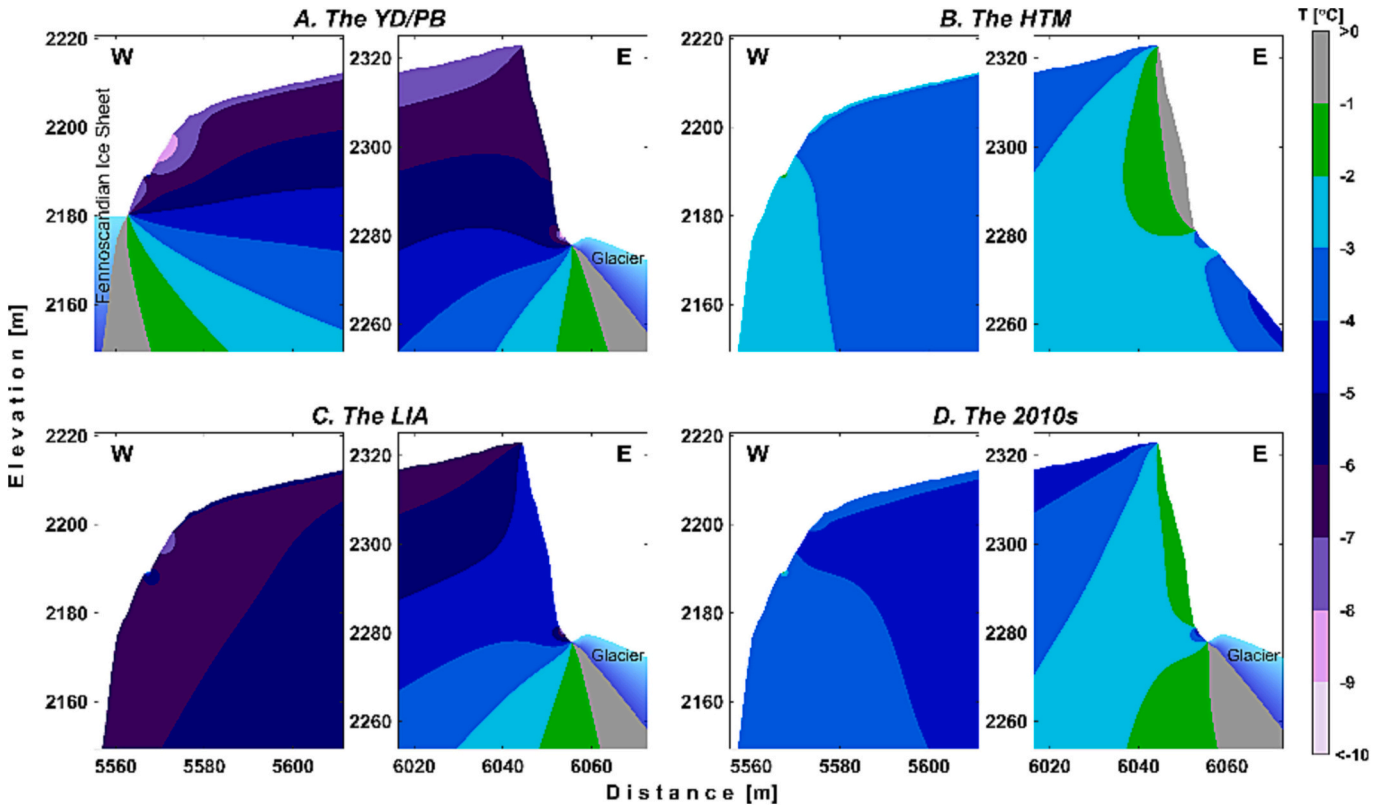

Fig. 5. Mean modeled ground temperature over four decennia: **A**. The Younger Dryas/Preboreal (YD/PB) transition, **B**. The Holocene Thermal Maximum (HTM), **C**. The Little Ice Age (LIA), and **D**. The 2010s.

gradients, resulting in large frost cracking potential. In addition, our assumption relating the snow distribution to slope gradient leads to a sharp transition in MAGST in the areas where slope gradient abruptly changes, and thus results in large thermal gradients in these areas close to the surface, where most frost cracking takes place. This is also the case between the blockfield and rock walls, where cornice snow may accumulate. The critical zones for enhanced frost weathering are most pronounced in the YD/PB and become weaker in the later periods. Nevertheless, they are still quite pronounced (e.g. the median crack radius simulations for the YD/PB vs HTM).

5. Discussion

5.1. Model limitations

We implemented two numerical models that each have their limitations: (1) a ground-temperature model, and (2) a frost-damage model. Both models are in two dimensions, which is an advance in comparison to one-dimensional models; however, the ground heat flow occurs in three dimensions in complex mountainous terrain (Noetzli and Gruber, 2009; Noetzli et al., 2007). Furthermore, uncertainties in the ground temperature modeling arise from our assumptions about the exclusively conductive heat transfer in the subsurface (i.e. neglecting advective heat transport from water fluxes), the model forcing, the assumed winter and summer surface offsets, and the assumed snow distribution (see more details in Czekirda et al., 2023). Furthermore, we assumed a simple parabolic ice-sheet profile during the YD and PB, which is certainly not always realistic (e.g. Patton et al., 2017; Stroeven et al., 2016), especially when ice flow is more governed by the subglacial topography during the thinning of the ice sheet with time. However, we assume the approach is sufficient for the aims and objectives of this study.

The employed frost damage model is a simple model that does not track the porosity evolution of individual cracks, as in e.g. Walder and Hallet (1986) or Sanders et al. (2012). The frost damage model instead focuses on larger geomorphological scales, and at the slope scale considered in our study, our choice of a simpler model is justified. The applied model is based on an assumed correlation between ice accumulation that is accommodated by porosity changes and frost damage. This reasoning is strictly justified when porosity changes due to non-reversible crack propagation are considered (Rempel et al., 2016), whereas more generally some poroelastic deformation is expected and could be relieved following thaw (Vlahou and Worster, 2010).

We note that the frost damage model was developed to describe fully saturated conditions and assumes that a water source is always available. Nevertheless, Rempel et al. (2016) argued that the porosity changes modeled in their study only required a small water supply from nearby pores and that this can be supplied by cannibalizing existing ice in regions where the ice pressure is insufficient to propagate cracks. The values of porosity changes modeled in our study are even smaller, hence the required water supply is quite small. Water flow is of central importance to the rock damage model, while in contrast, the thermal model assumes that water movement is unimportant as a heat transport mechanism because conductive transport can take place through the entire rock volume, whereas advective heat transport is constrained by relatively small pore volumes and low Darcy transport rates (i.e. the thermal *Peclet* number is small). Put another way, water flow and freezing of water drawn to the freezing front are important at the crack scale; however, they are omitted in the model scale of meters and tens of meters. As the small cracks comprise only a very small volume of a block, the impact on the freezing dynamics is negligible. In addition, ice segregation occurs at quite low ground temperatures in our study, hence the water movement at a larger scale is limited and its influence on the ground temperature is likely of minor importance.

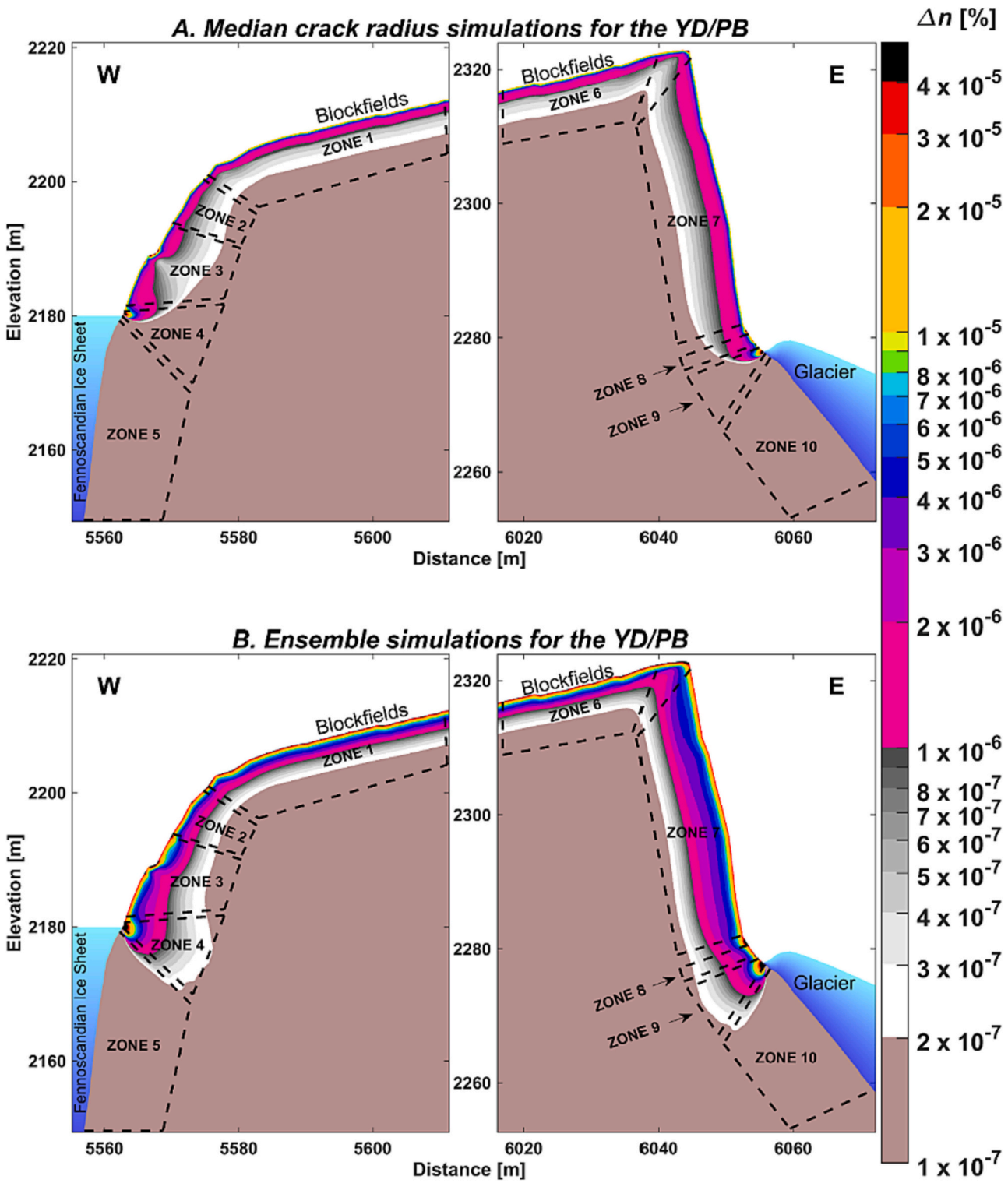

Fig. 6. Porosity changes Δ*n* in the Veslpiggen Plateau over the Younger Dryas/Preboreal (YD/PB) transition computed based on the undercooling for frost cracking for: **A**: Median crack radius simulations. **B**: Ensemble simulations. Note the logarithmic scale.

5.2. *Model improvements and their feasibility*

The main difference between this study using the 2D approach and other studies using the 1D approach (Draebing et al., 2022; Hales and Roering, 2007; Rempel et al., 2016; Savi et al., 2015) is that the lateral effects across areas with high thermal gradients could be simulated. Myhra et al. (2019) modeled large thermal gradients between the shaded rock walls and talus slopes below based on the conductive 2D ground temperature modeling, implying that frost weathering may be very active in such transition zones. Berrisford (1991)'s investigations suggested a high potential for weathering at the average annual retreat position for snow patches in Jotunheimen. Furthermore, this finding is crucial for supporting the nivation processes and associated landforms (Christiansen, 1998). In our modeling, sharp transitions in snow depth

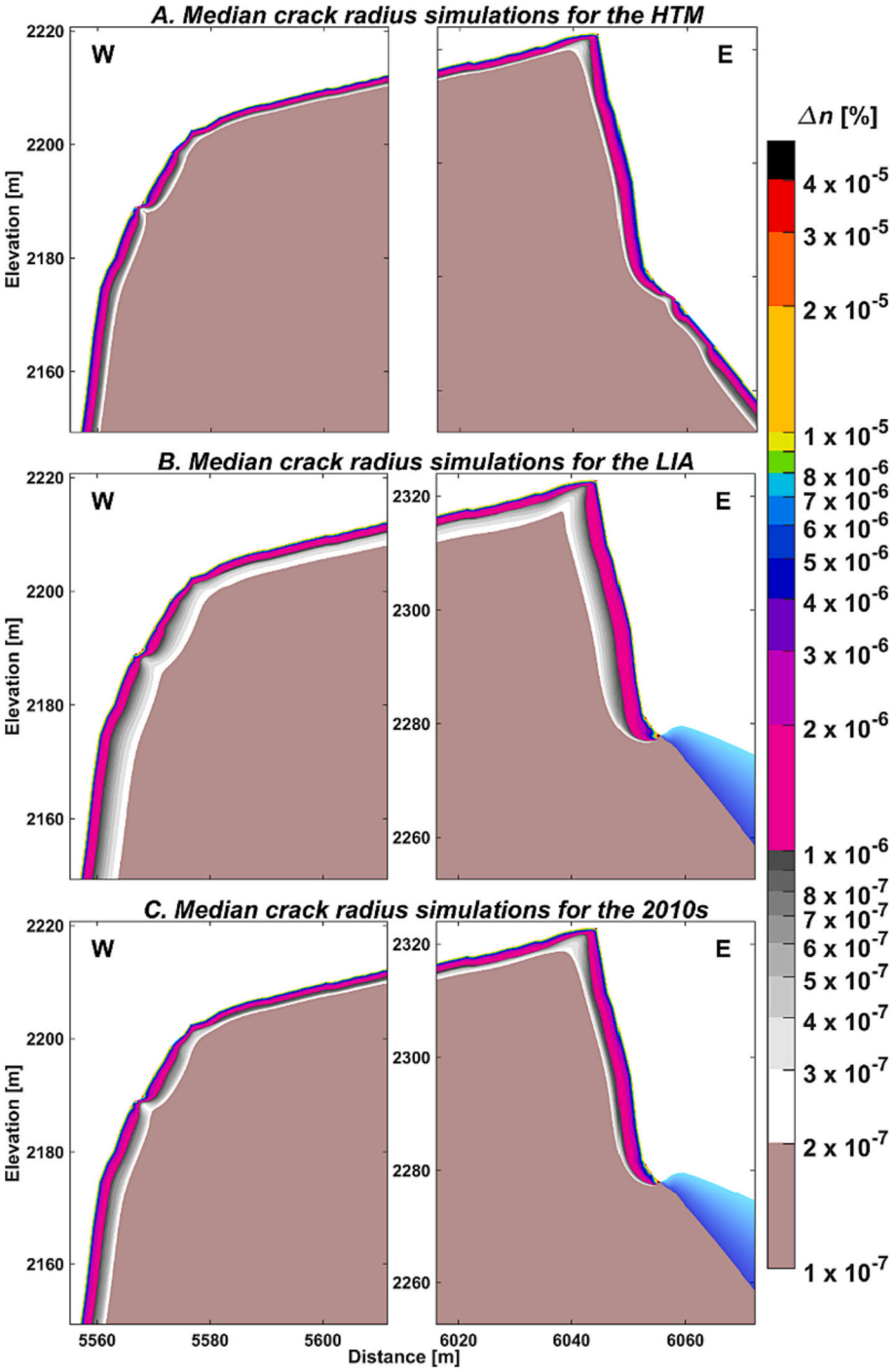

Fig. 7. Porosity changes Δ*n* in the Veslpiggen Plateau computed based on undercooling for frost cracking for the median crack radius for various decennia. HTM – The Holocene Thermal Maximum. LIA – The Little Ice Age. Note the logarithmic scale.

along the profiles led to quite large thermal gradients, indicating that spatial heterogeneities in snow cover could be sufficient to generate transition zones with elevated frost damage. The latter is in accordance with the studies of coastal cliff temperatures in Svalbard, where larger frost weathering potential is related to thermal gradients due to snow cover variations (Ødegård et al., 1995; Ødegård and Sollid, 1993). Furthermore, the most pronounced frost weathering potential is modeled between glaciers and rock walls in our study, which agrees well with the study of Hartmeyer et al. (2020) concerning glaciated cirques in the Central Alps of Austria, where ice segregation led to high rockfall activity in recently deglaciated areas.

To our knowledge, no other frost weathering modeling study to date has attempted to account for heterogenous crack radii. We did not attempt to fully describe interactions between cracks, although we recognize that liquid water is likely to be redistributed between various cracks according to their sizes, and not necessarily only according to their temperatures. As ground temperature drops, ice growth is expected to start in the largest cracks, and subsequently in smaller ones with progressing temperature decrease (Anderson et al., 2013). Frost damage would also start in the largest cracks because the smaller cracks require greater ice pressure to grow (Rempel et al., 2016), hence their undercooling for frost cracking has larger values (Fig. 4). However, it is

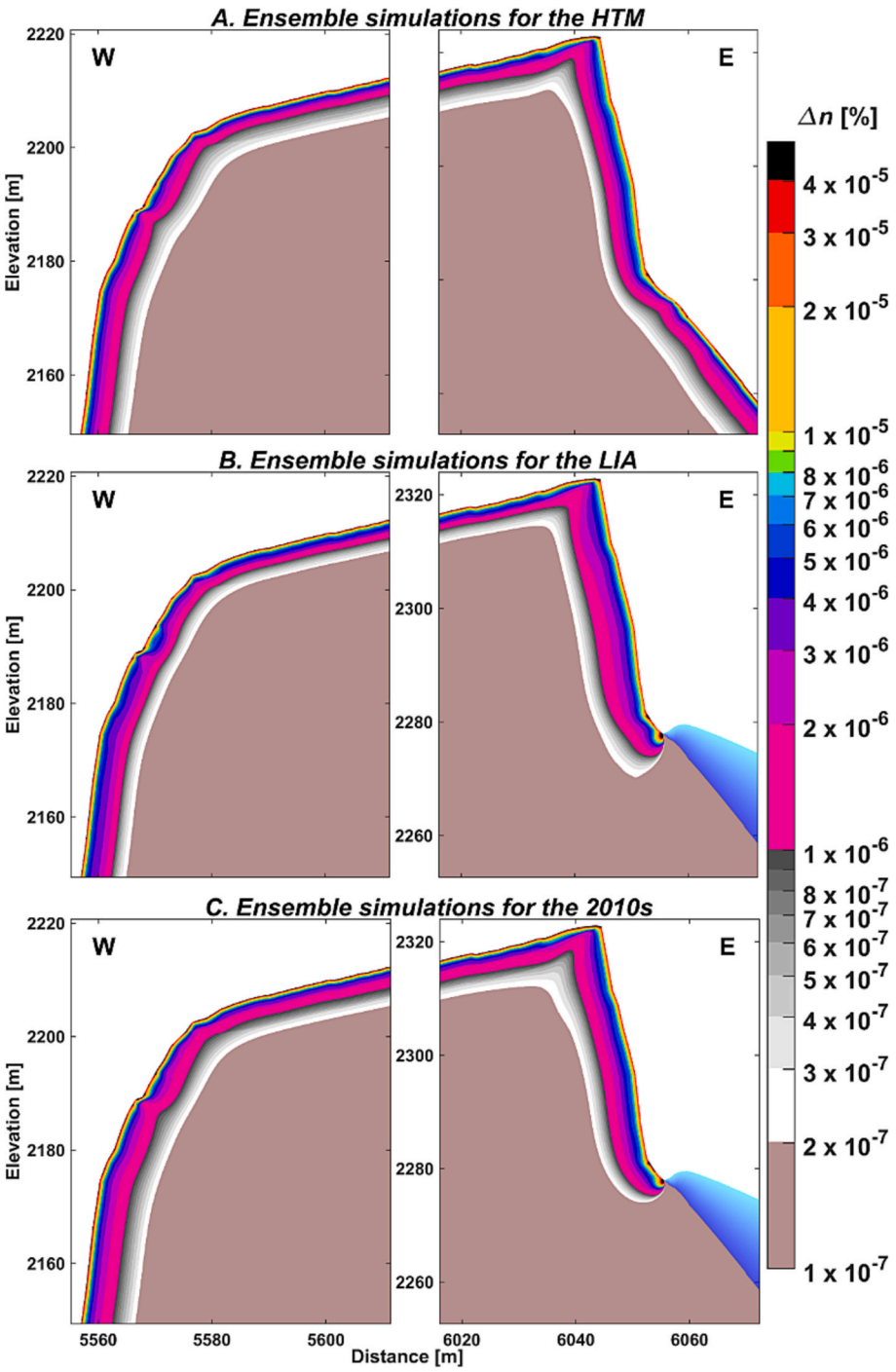

Fig. 8. Porosity changes Δn in the Veslpiggen Plateau computed based on undercooling for frost cracking from the ensemble simulations for various decennia. HTM – The Holocene Thermal Maximum. LIA – The Little Ice Age. Note the logarithmic scale.

uncertain whether liquid water would feed the smaller cracks at lower ground temperatures, because the larger cracks may suck water from the smaller cracks, as laboratory experiments suggest for isothermal frost damage (Rempel and Van Alst, 2013). The mean values from the ensemble approach are governed by larger crack radii than the median crack radius, which might be viewed as suggestive of such a water redistribution process, although we emphasize that our approach was not formulated to account explicitly for such crack growth interactions. Further model developments are needed to better account for the interaction of the various crack radii, ideally tested by laboratory experiments or field observations, although the collection of suitable validation data may be challenging, as shown in other frost weathering studies (Matsuoka and Murton, 2008).

5.3. Spatiotemporal distribution of frost damage

In general, studies show that frost weathering is more intense in north-facing rock walls since they have lower ground temperatures and may have higher moisture content (Coutard and Francou, 1989; Sass, 2005a). Even though we cannot discuss the relevance of moisture content, our results showed that the sun-exposed rock walls should have more frost damage, in agreement with Draebing and Mayer (2021), who

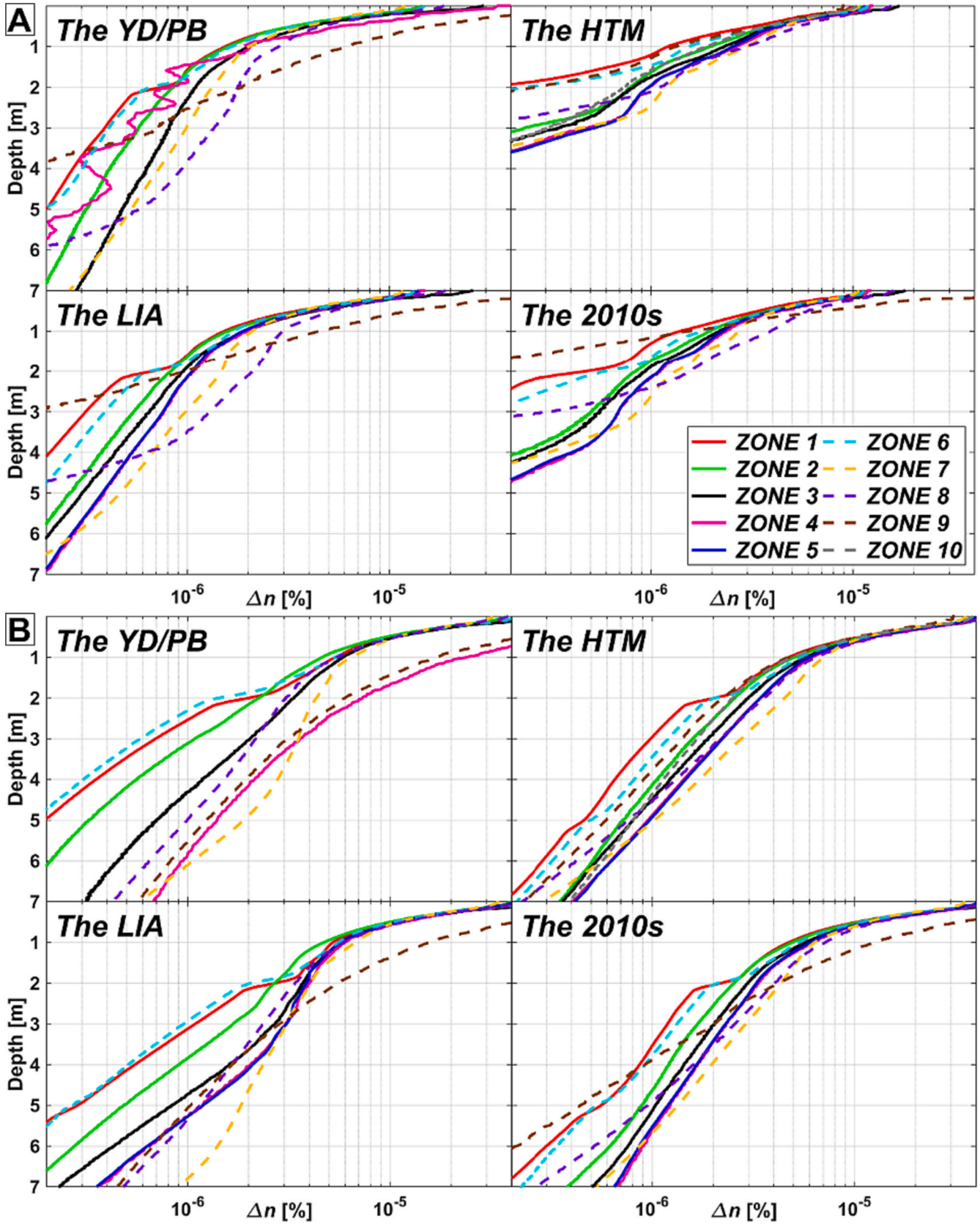

Fig. 9. Average profiles of porosity change Δ*n* with depth in zones shown in Fig. 6 for: **A**: Median crack radius simulations. **B**: Ensemble simulations. YD/PB – The Younger Dryas/Preboreal. HTM – The Holocene Thermal Maximum. LIA – The Little Ice Age. Note the logarithmic scale.

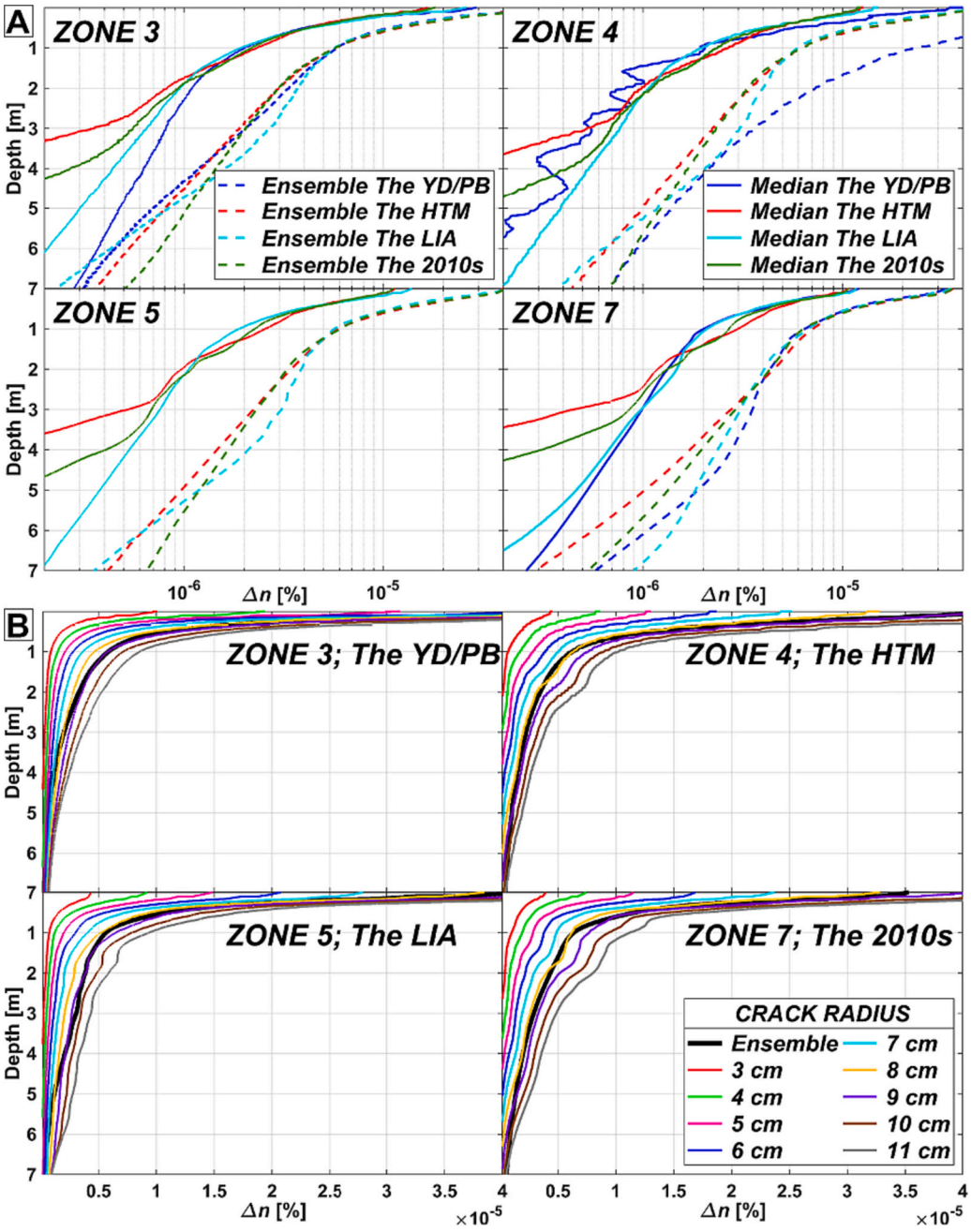

Fig. 10. Average profiles of porosity change Δn with depth in zones encompassing rock walls shown in Fig. 6. **A**: Temporal changes in each zone. Note the logarithmic scale. **B**: Simulations for various crack radii and ensemble simulations. YD/PB – The Younger Dryas/Preboreal. HTM – The Holocene Thermal Maximum. LIA – The Little Ice Age.

also used the model by Rempel et al. (2016). The large frost cracking potential in the east-facing rock wall in Jotunheimen likely arises from the largest MAGST amplitudes in this exposition. The latter is retained from the original 1D frost damage model as shown in the examples by Rempel et al. (2016). We also showed that rock walls have generally more effective frost cracking than other terrain types due to the largest MAGST amplitudes. Our modeling could be extended by running the model at sub-daily time steps to further show that also sub-daily temperature variations would be larger in rock walls than in other terrain types, where deeper snow cover decreases daily temperature amplitudes (e.g. Anderson et al., 2013).

The warmest modeled period of the HTM was the period with the smallest frost-weathering potential in the rock walls, according to both the median crack radius and ensemble simulations. The ongoing atmospheric warming will soon bring climatic conditions to those in the HTM, implying that frost weathering potential in the rock walls in Jotunheimen will be reduced in the future. Kellerer-Pirklbauer (2017) discussed a similar future with smaller frost weathering in the rock walls in the Alps in Austria.

5.4. Geomorphological implications

Frost weathering plays an important role in rock wall retreat and comprises a large contribution to rockfall supply onto talus slopes (Krautblatter and Dikau, 2007). Frost weathering leads to intensification of rockfall processes (Blikra and Nemec, 1998), although in detail segregation ice weathering acts primarily as a preconditioning mechanism (Curry, 2023), enabling rockfall events to be triggered by other

factors such as seasonal thawing of the active layer as segregation ice melts out (Sass, 2005b), deepening of the active layer (Gruber et al., 2004; Ravanel and Deline, 2011), adverse weather such as persistent heavy rainfall and snowmelt (Sandersen et al., 1997), or earthquakes that may result from enhanced seismic activity during glacio-isostatic rebound (Bellwald et al., 2019; Cossart et al., 2014). Frost weathering has been mentioned as a possible destabilizing factor for rock avalanches in Norway by Blikra et al. (2006), although it is uncertain whether frost weathering contributes to larger events, because frost weathering processes operate mostly in the upper few meters (Krautblatter et al., 2013; Rempel et al., 2016), as our results also suggest. Hence, larger rock slope failures in permafrost-underlain terrain are much more influenced by long-term permafrost changes, and the delay in the rock material release may be as long as millennia when permafrost finally degrades (Matthews et al., 2018; Hilger et al., 2021). Rockfalls often recur seasonally and therefore we assume they are much more related to the frost weathering processes in periglacial environments.

According to our results, the frost weathering potential was largest between the relatively warmer ice sheets or glaciers and relatively colder rock walls or moderately steep slopes in the YD/PB, when ground temperatures were lowest since deglaciation. This aspect agrees well with the knowledge about rockfall accumulations outside Norway since deglaciation, i.e. that most sediments accumulated soon after deglaciation (e.g. Rapp, 1960; Ballantyne and Kirkbride, 1987; Hinchliffe and Ballantyne, 1999), although it is uncertain whether these sediments should be considered as due to stress release in response to deglaciation or periglacial due to the enhanced frost weathering (Ballantyne, 2002; Ballantyne and Harris, 1994; Hinchliffe and Ballantyne, 1999). However, the mentioned processes may be connected. Rock walls affected by glacial debuttressing would be highly fractured near the surface, priming them for even more efficient frost weathering (Ballantyne and Kirkbride, 1987; Hales and Roering, 2009). Messenzehl et al. (2017) investigated the influence of various factors on rockfall distribution at a regional scale in the Turtmann Valley in the Swiss Alps. They concluded that ice segregation is probably the most important breakdown mechanism in the study area, even more important than time since deglaciation and mechanical factors, implying that debuttressing effects may be overestimated in some areas. Other studies focus on more intense ice segregation weathering as permafrost aggrades during deglaciation (e.g. Draebing et al., 2022). Our results indicate potentially large periglacial activity in rock walls during deglaciation, specifically where large temperature differences exist between rock walls and melting ice sheets or glaciers. The results suggest not only a large frost cracking potential close to the surface, but also possibly a larger frost weathering potential at depth in such areas. The enhanced frost weathering at sites with large thermal gradients could progressively weaken entire rock walls during an ice sheet/glacier retreat, when abundant meltwater would be available from the melting ice sheet/glacier. Ongoing glacier retreat already increases rockfalls from newly deglaciated rock wall faces in the European Alps (Fischer et al., 2006) and in the Peruvian Andes (Stuart-Smith et al., 2021), perhaps partly due to meltout or warming of ice lenses formed in rock faces adjacent to previous glacier surfaces.

In southern Norway, most rockfall material accumulated during the climatic deterioration over the YD (Blikra and Nemec, 1998) and generally after deglaciation (Matthews and Nesje, 2023). Those studies compare favorably with the large frost cracking in the YD modeled in our study. The enhanced frost weathering at that time was likely also important for the development of relict talus-derived rock glaciers in Norway (Lilleøren and Etzelmüller, 2011). Blikra and Longva (1995) discussed that the Quaternary deposits in the Møre-Romsdal district in Norway probably accumulated due to intense frost weathering in the YD with deep permafrost conditions. The early Holocene and the HTM were probably periods with limited rockfall activity (Blikra and Nemec, 1998), which coincides with the lowest modeled frost cracking potential during the HTM in our study. The rockfall activity increased again in the second half of the Holocene (Blikra and Nemec, 1998; Nesje, 2002; Nesje et al., 1994), likely due to climatic deterioration and hence the increased frost weathering activity during colder and perhaps wetter phases of the mid-Holocene (Neo-glaciation). Several rockfall events and colluvial processes occurred in Jotunheimen during the late Holocene over the last 4000 years (Støren et al., 2008). Our results could explain more intense periglacial weathering in the relatively colder climate of the LIA. McCarroll et al. (2001)'s study claimed that rockfall accumulation rates in the Jotunheimen region were substantially higher in the coldest phase of the LIA, implying that periglacial processes and thus climate variations are sufficient to explain the origin of the talus in this area with no need for glacial debuttressing effects. In a transition period, heat waves may exert a particularly strong influence on the stability of steep rock walls as long as parts of the rock wall are frozen. The timing of small rock-slope failures (excluding rockfalls) in the Jotunheimen area was different than the mentioned rockfall activity and peaked in the mid- to late-Holocene due to permafrost degradation (Matthews et al., 2018).

Frost weathering has long been an interest within the research on the development of glacial cirques, where the bergschrund, the randkluft or both have been identified as the key locations for effective erosion in lower parts of headwalls (e.g. Gardner, 1987; Evans, 2021). In such zones, intensely frost-weathered material is further transported by glacier through quarrying, thereby allowing for high erosion rates in glaciated cirques. Thermal conditions in such zones are certainly important for cirque erosion and the variations in elevation of glacier surfaces led to the exposure of several hundred meters of cirque headwalls to frost weathering throughout the Quaternary (Gardner, 1987). One-dimensional modeling of ice segregation weathering has already been proven to be useful for understanding the role of frost weathering in cirque erosion (Sanders et al., 2012). Further attempts using the two-dimensional approach as shown here may allow for even more progress, as large thermal gradients along cirque headwall are probable (e.g. Fisher, 1955).

6. Conclusions

We have modeled ground temperature in two dimensions in a mountain plateau in the Jotunheimen Mountains in Norway. Based on the modeled thermal fields, we computed frost damage potential in 2D using an established numerical model. We derived and presented the first frost cracking index applied to rock walls in two dimensions. In addition, we mapped crack radii in a nearby rock wall and ran ensemble simulations to account for the distribution of crack radii. We demonstrated limitations of the modeling and highlighted the importance of developing more advanced frost cracking indices that account more fully for interactions between populations of crack radii in rock walls and their two-/three-dimensional nature.

The key findings of our modeling are summarized as follows:

(1) Sites of enhanced frost weathering are concentrated in the vicinity of the melting ice sheet, the local glaciers and anywhere else where sharp transitions in snow conditions occur, resulting in large temperature gradients in these areas.
(2) Sites of enhanced frost weathering due to lateral effects are not strongly controlled by the climatic conditions as long as they are within the periglacial domain. However, the location of such sites changes due to evolving snow and glacier coverage.
(3) If only one crack radius is modeled, we recommend replacing the median crack radius with a larger crack radius, since ice growth in larger cracks can be more effective at promoting frost damage.
(4) Simulated porosity changes indicate that in addition to glacial debuttressing processes, frost weathering can weaken the bedrock while the ice sheet/glacier melts. This could be particularly important both for deglaciation and ongoing contemporary mountain glacier retreat around the world, and could potentially increase material detachability from rock faces in newly deglaciated areas.

(5) Our modeled frost weathering potential compares favorably with most of the published studies concerning the timing of rockfall accumulations in southern Norway.

Funding

This study was funded through Justyna Czekirda's doctoral research fellow position at the Department of Geosciences, University of Oslo, Norway.

CRediT authorship contribution statement

Justyna Czekirda: Conceptualization, Formal analysis, Methodology, Software, Visualization, Writing – original draft. **Alan W. Rempel:** Conceptualization, Formal analysis, Methodology, Writing – review & editing. **Bernd Etzelmüller:** Conceptualization, Methodology, Supervision, Writing – review & editing. **Sebastian Westermann:** Methodology, Writing – review & editing.

Declaration of competing interest

The authors declare that they have no known competing financial interests or personal relationships that could have appeared to influence the work reported in this paper.

Data availability

Data will be made available on request.

Acknowledgments

We thank Luc Girod for collecting drone imagery from the Kjelen rock wall and Trond Eiken for additional help during the fieldwork.

Appendix A. Frost damage model derivation

In the present study, we model the porosity changes using Supplementary Eq. (5) in Rempel et al. (2016), which is applicable to two- and three-dimensional cases:

$$\frac{\partial n}{\partial t} = \frac{\rho L}{T_m \mu}\left[\frac{dk}{dT}\,(\nabla T)^2 + k\nabla^2 T\right], \tag{A.1}$$

where n is the porosity, ρ is the ice density (920 kg m^{-3}), L is the specific latent heat of fusion for water (334 kJ kg^{-1}), T_m is the bulk melting temperature (273.15 K), and μ is the water dynamic viscosity (here 1.8 mPa s). The temperature-dependent permeability $k(T)$ is parametrized using the power-law function:

$$k(T) = k_c\left(\frac{\Delta T_c}{\Delta T}\right)^{\alpha} \tag{A.2}$$

where α is the unitless power-law exponent between 2 and 5, k_c denotes the permeability at ΔT_c, typically between 10^{-24} and 10^{-16} m^2. ΔT_c is the upper-temperature limit for frost cracking. The first derivative of $k(T)$ with respect to T is:

$$\frac{dk(T)}{dT} = \frac{k_c \alpha}{\Delta T_c}\left(\frac{\Delta T_c}{\Delta T}\right)^{\alpha+1} \tag{A.3}$$

Using Eqs. (A.2) and (A.3) in Eq. (A.1), we may then express:

$$\frac{\partial n}{\partial t} = \frac{\alpha \rho L k_c}{T_m \mu \Delta T_c}\left(\frac{\Delta T_c}{\Delta T}\right)^{\alpha+1}(\nabla T)^2 + \frac{\rho L k_c}{T_m \mu}\left(\frac{\Delta T_c}{\Delta T}\right)^{\alpha}\nabla^2 T \tag{A.4}$$

where D – "the frost weathering diffusivity" is:

$$D = \frac{\alpha \rho L k_c \Delta T_c}{T_m \mu} \tag{A.5}$$

Using Eq. (A.5) in Eq. (A.4), we find:

$$\frac{\partial n}{\partial t} = \frac{D\Delta {T_c}^{\alpha-1}\Delta T^{-\alpha}}{\alpha}\left[\frac{\alpha}{\Delta T}\,(\nabla T)^2 + \nabla^2 T\right] \tag{A.6}$$

For a node in two dimensions with the Cartesian coordinates x and y at the time t, the model for porosity changes becomes:

$$\Delta n(x,y,t) = \frac{D\Delta {T_c}^{\alpha-1}}{\alpha}\int_{t_c}^{t}\Delta T(x,y,t)^{-\alpha}\left[\frac{\alpha}{\Delta T(x,y,t)}\,(\nabla T(x,y,t))^2 + \nabla^2 T(x,y,t)\right]dt \tag{A.7}$$

The accumulated porosity change for one year can thus be written as:

$$\Delta n(x,y) = \frac{D\Delta {T_c}^{\alpha-1}}{\alpha}\int_{\Delta T>\Delta T_c,1\ year}\Delta T(x,y)^{-\alpha}\left[\frac{\alpha}{\Delta T(x,y)}\,(\nabla T(x,y))^2 + \nabla^2 T(x,y)\right]dt \tag{A.8}$$

References

Anderson, R.S., 1998. Near-surface thermal profiles in alpine bedrock: implications for the frost weathering of rock. Arctic and Alpine Research 30 (4), 362–372. https://doi.org/10.2307/1552008.

Anderson, R.S., Anderson, S.P., Tucker, G.E., 2013. Rock damage and regolith transport by frost: an example of climate modulation of the geomorphology of the critical zone. Earth Surf Proc Land 38 (3), 299–316. https://doi.org/10.1002/esp.3330.

André, M.-F., 2003. Do periglacial landscapes evolve under periglacial conditions? Geomorphology 52 (1–2), 149–164. https://doi.org/10.1016/s0169-555x(02)00255-6.

Ballantyne, C.K., 2002. Paraglacial geomorphology. Quaternary Science Reviews 21 (18), 1935–2017. https://doi.org/10.1016/S0277-3791(02)00005-7.

Ballantyne, C.K., 2018. Periglacial Geomorphology. Wiley-Blackwell.

Ballantyne, C.K., Harris, C., 1994. The periglaciation of Great Britain. UK:Cambridge University Press, Cambridge.

Ballantyne, C.K., Kirkbride, M.P., 1987. Rockfall activity in upland britain during the loch lomond stadial. Geogr J. 153 (1), 86–92. https://doi.org/10.2307/634474.

Bellwald, B., Hjelstuen, B.O., Sejrup, H.P., Stokowy, T., Kuvås, J., 2019. Holocene mass movements in west and mid-Norwegian fjords and lakes. Mar. Geol. 407, 192–212. https://doi.org/10.1016/j.margeo.2018.11.007.

Berrisford, M.S., 1991. Evidence for enhanced mechanical weathering associated with seasonally late-lying and perennial snow patches, Jotunheimen. Norway. Permafrost Periglac 2 (4), 331–340. https://doi.org/10.1002/ppp.3430020408.

Berthling, I., Etzelmüller, B., 2011. The concept of cryo-conditioning in landscape evolution. Quatern. Res. 75 (2), 378–384. https://doi.org/10.1016/j.yqres.2010.12.011.

Blikra, L.H., Longva, O., 1995. Frost-shattered debris facies of Younger Dryas age in the coastal sedimentary successions in western Norway: palaeoenvironmental implications. Palaeogeogr. Palaeoclimatol. Palaeoecol. 118 (1), 89–110. https://doi.org/10.1016/0031-0182(94)00141-T.

Blikra, L.H., Nemec, W., 1998. Postglacial colluvium in western Norway: depositional processes, facies and palaeoclimatic record. Sedimentology 45 (5), 909–960. https://doi.org/10.1046/j.1365-3091.1998.00200.x.

Blikra, L.H., Longva, O., Braathen, A., Anda, E., Dehls, J., Stalsberg, K., 2006. Rock slope failures in Norwegian fjord areas: Examples, spatial distribution and temporal pattern. In: Landslides from Massive Rock Slope Failure. Springer, pp. 475–496.

Boeckli, L., Brenning, A., Gruber, S., Noetzli, J., 2012. A statistical approach to modelling permafrost distribution in the European Alps or similar mountain ranges. Cryosphere 6 (1), 125–140. https://doi.org/10.5194/tc-6-125-2012.

Carslaw, H.S., Jaeger, J.C., 1959. Conduction of Heat in Solids. Clarendon Press.

Chang, S.-H., Lee, C.-I., Jeon, S., 2002. Measurement of rock fracture toughness under modes I and II and mixed-mode conditions by using disc-type specimens. Eng. Geol. 66 (1), 79–97. https://doi.org/10.1016/S0013-7952(02)00033-9.

Christiansen, H.H., 1998. Nivation forms and processes in unconsolidated sediments. NE Greenland. Earth Surf Proc Land 23 (8), 751–760. https://doi.org/10.1002/(SICI)1096-9837(199808)23:8<751::AID-ESP886>3.0.CO;2-A.

Cossart, E., Mercier, D., Decaulne, A., Feuillet, T., Jónsson, H.P., Sæmundsson, Þ., 2014. Impacts of post-glacial rebound on landslide spatial distribution at a regional scale in northern Iceland (Skagafjörður). Earth Surf. Process. Landforms 39, 336–350. https://doi.org/10.1002/esp.3450.

Coutard, J.-P., Francou, B., 1989. Rock temperature measurements in two alpine environments: implications for frost shattering. Arctic and Alpine Research 21 (4), 399–416. https://doi.org/10.2307/1551649.

Curry, A., 2023. Talus slopes. In *Reference Module in Earth Systems and Environmental Sciences. Elsevier.* https://doi.org/10.1016/B978-0-323-99931-1.00047-7.

Czekirda, J., Etzelmüller, B., Westermann, S., Isaksen, K., Magnin, F., 2023. Post-Little Ice Age rock wall permafrost evolution in Norway. The Cryosphere 17 (7), 2725–2754. https://doi.org/10.5194/tc-17-2725-2023.

Dash, J.G., Rempel, A.W., Wettlaufer, J.S., 2006. The physics of premelted ice and its geophysical consequences. Rev. Mod. Phys. 78 (3), 695–741. https://doi.org/10.1103/RevModPhys.78.695.

Draebing, D., Mayer, T., 2021. Topographic and geologic controls on frost cracking in Alpine rockwalls. J. Geophys. Res. Earth 126 (6), e2021JF006163. https://doi.org/10.1029/2021JF006163.

Draebing, D., Mayer, T., Jacobs, B., McColl, S.T., 2022. Alpine Rockwall erosion patterns follow elevation-dependent climate trajectories. Communications Earth & Environment 3 (1), 21. https://doi.org/10.1038/s43247-022-00348-2.

Duca, S., Occhiena, C., Mattone, M., Sambuelli, L., Scavia, C., 2014. Feasibility of ice segregation location by acoustic emission detection: A laboratory test in gneiss. Permafrost Periglac 25 (3), 208–219. https://doi.org/10.1002/ppp.1814.

Egholm, D.L., Andersen, J.L., Knudsen, M.F., Jansen, J.D., Nielsen, S.B., 2015. The periglacial engine of mountain erosion – part 2: Modelling large-scale landscape evolution. Earth Surf. Dynam. 3 (4), 463–482. https://doi.org/10.5194/esurf-3-463-2015.

Evans, I.S., 2021. Glaciers, rock avalanches and the 'buzzsaw' in cirque development: why mountain cirques are of mainly glacial origin. Earth Surf. Process. Landforms 46, 24–46. https://doi.org/10.1002/esp.4810.

Farbrot, H., Etzelmüller, B., Gudmundsson, A., Humlum, O., Kellerer-Pirklbauer, A., Eiken, T., Wangensteen, B., 2007. Rock glaciers and permafrost in Tröllaskagi, Northern Iceland. Zeitschrift für Geomorphologie, Supplementary Issues 51, 1–16. https://doi.org/10.1127/0372-8854/2007/0051S2-0001.

Farbrot, H., Hipp, T.F., Etzelmüller, B., Isaksen, K., Ødegård, R.S., Schuler, T.V., Humlum, O., 2011. Air and ground temperature variations observed along elevation and continentality gradients in Southern Norway. Permafrost Periglac 22 (4), 343–360. https://doi.org/10.1002/ppp.733.

Fischer, L., Kääb, A., Huggel, C., Noetzli, J., 2006. Geology, glacier retreat and permafrost degradation as controlling factors of slope instabilities in a high-mountain rock wall: the Monte Rosa east face. Nat. Hazards Earth Syst. Sci. 6 (5), 761–772. https://doi.org/10.5194/nhess-6-761-2006.

Fischer, L., Purves, R.S., Huggel, C., Noetzli, J., Haeberli, W., 2012. On the influence of topographic, geological and cryospheric factors on rock avalanches and rockfalls in high-mountain areas. Nat Hazard Earth Sys 12 (1), 241–254. https://doi.org/10.5194/nhess-12-241-2012.

Fisher, J.E., 1955. Internal Temperatures of a Cold Glacier and Conclusions Therefrom. Journal of Glaciology 2 (18), 583–591. https://doi.org/10.3189/002214355793702163.

Fredin, O., Bergstrøm, B., Eilertsen, R., Hansen, L., Longva, O., Nesje, A., & Sveian, H. (2013). Glacial landforms and Quaternary landscape development in Norway. *Quaternary Geology of Norway, edited by: Olsen, L., Fredin, O., and Olesen, O., Geological Survey of Norway Special Publication, Geological Survey of Norway, Trondheim, 525.*

French, H.M., 2016. Do periglacial landscapes exist? A discussion of the upland landscapes of northern interior Yukon. Canada. Permafrost Periglac 27 (2), 219–228. https://doi.org/10.1002/ppp.1866.

Gardner, J.S., 1987. Evidence for Headwall Weathering zones, Boundary Glacier, Canadian Rocky Mountains. J. Glaciol. 33 (113), 60–67. https://doi.org/10.3189/S0022143000005359.

Gruber, S., Haeberli, W., 2007. Permafrost in steep bedrock slopes and its temperature-related destabilization following climate change. J Geophys Res-Earth 112 (F2). https://doi.org/10.1029/2006jf000547.

Gruber, S., Hoelzle, M., Haeberli, W., 2004. Permafrost thaw and destabilization of Alpine rock walls in the hot summer of 2003. Geophys. Res. Lett. 31 (13) https://doi.org/10.1029/2004gl020051.

Hales, T.C., Roering, J.J., 2007. Climatic controls on frost cracking and implications for the evolution of bedrock landscapes. J. Geophys. Res. Earth 112 (F2). https://doi.org/10.1029/2006JF000616.

Hales, T.C., Roering, J.J., 2009. A frost "buzzsaw" mechanism for erosion of the eastern Southern Alps. New Zealand. Geomorphology 107 (3), 241–253. https://doi.org/10.1016/j.geomorph.2008.12.012.

Hallet, B., Walder, J.S., Stubbs, C.W., 1991. Weathering by segregation ice growth in microcracks at sustained subzero temperatures: Verification from an experimental study using acoustic emissions. Permafrost Periglac 2 (4), 283–300. https://doi.org/10.1002/ppp.3430020404.

Hanssen, T.H., 1988. Rock properties. In: Norwegian Tunnelling Today, vol. Publication No. 5. Tapir Publishers, University of Trondheim, pp. 41–44.

Hanssen-Bauer, I., Tveito, O., Szewczyk-Bartnicka, H., 2006. Comparison of grid-based and station-based regional temperature and precipitation series. *Met.No Report, 4/2006*. Retrieved from. https://www.met.no/publikasjoner/met-report/met-report-2006/_/attachment/download/dd9d9481-5986-4790-9154-54dd5a4ceae7:4b95bfe33dcc6651f34bed4e1e36399cb19bbdef/MET-report-04-2006.pdf.

Harris, C., Haeberli, W., Vonder Mühll, D., King, L., 2001. Permafrost monitoring in the high mountains of Europe: the PACE Project in its global context. Permafrost Periglac 12 (1), 3–11. https://doi.org/10.1002/ppp.377.

Hartmeyer, I., Delleske, R., Keuschnig, M., Krautblatter, M., Lang, A., Schrott, L., Otto, J. C., 2020. Current glacier recession causes significant rockfall increase: the immediate paraglacial response of deglaciating cirque walls. Earth Surf. Dynam. 8 (3), 729–751. https://doi.org/10.5194/esurf-8-729-2020.

Hilger, P., Hermanns, R.L., Czekirda, J., Myhra, K.S., Gosse, J.C., Etzelmüller, B., 2021. Permafrost as a first order control on long-term rock-slope deformation in (Sub-) Arctic Norway. Quat. Sci. Rev. 251, 106718. https://doi.org/10.1016/j.quascirev.2020.106718.

Hinchliffe, S., Ballantyne, C.K., 1999. Talus accumulation and Rockwall retreat, Trotternish, Isle of Skye. Scotland. Scottish Geographical Journal 115 (1), 53–70. https://doi.org/10.1080/00369229918737057.

Hipp, T., Etzelmüller, B., Westermann, S., 2014. Permafrost in Alpine Rock Faces from Jotunheimen and Hurrungane. Southern Norway. *Permafrost Periglac* 25 (1), 1–13. https://doi.org/10.1002/ppp.1799.

Hughes, A.L.C., Gyllencreutz, R., Lohne, Ø.S., Mangerud, J., Svendsen, J.-I., 2015. DATED-1: Compilation of Dates and Time-slice Reconstruction of the Build-up and Retreat of the Last Eurasian (British-Irish, Scandinavian, Svalbard-Barents-Kara Seas) Ice Sheets 40-10 ka. Department of Earth Science, University of Bergen and Bjerknes Centre for Climate Research, PANGAEA [dataset]. https://doi.org/10.1594/PANGAEA.848117.

Kellerer-Pirklbauer, A., 2017. Potential weathering by freeze-thaw action in alpine rocks in the European Alps during a nine year monitoring period. Geomorphology 296, 113–131. https://doi.org/10.1016/j.geomorph.2017.08.020.

Kleman, J., Stroeven, A.P., Lundqvist, J., 2008. Patterns of Quaternary ice sheet erosion and deposition in Fennoscandia and a theoretical framework for explanation. Geomorphology 97 (1), 73–90. https://doi.org/10.1016/j.geomorph.2007.02.049.

Krautblatter, M., Dikau, R., 2007. Towards a uniform concept for the comparison and extrapolation of Rockwall retreat and rockfall supply. Geogr. Ann. Ser. B 89 (1), 21–40. https://doi.org/10.1111/j.1468-0459.2007.00305.x.
Krautblatter, M., Funk, D., Günzel, F.K., 2013. Why permafrost rocks become unstable: a rock-ice-mechanical model in time and space. Earth Surf Proc Land 38 (8), 876–887. https://doi.org/10.1002/esp.3374.
Lilleøren, K.S., Etzelmüller, B., 2011. A regional inventory of rock glaciers and ice-cored moraines in Norway. Geogr. Ann. Ser. B 93 (3), 175–191. https://doi.org/10.1111/j.1468-0459.2011.00430.x.
Lilleøren, K.S., Etzelmüller, B., Schuler, T.V., Gisnås, K., Humlum, O., 2012. The relative age of mountain permafrost — estimation of Holocene permafrost limits in Norway. Global Planet. Change 92-93, 209–223. https://doi.org/10.1016/j.gloplacha.2012.05.016.
Liu, Z., Otto-Bliesner, B.L., He, F., Brady, E.C., Tomas, R., Clark, P.U., Carlson, A.E., Lynch-Stieglitz, J., Curry, W., Brook, E., Erickson, D., Jacob, R., Kutzbach, J., Cheng, J., 2009. Transient simulation of last deglaciation with a new mechanism for Bølling-Allerød warming. Science 325 (5938), 310–314. https://doi.org/10.1126/science.1171041.
Lussana, C., 2020. *seNorge observational gridded datasets. seNorge_2018, version 20.05*. [dataset]. https://arxiv.org/abs/2008.02021.
Lutro, O., & Tveten, E. (2012). Berggrunnskart (EN Bedrock map) Galdhøpiggen 1518 II, M 1: 50.000. Retrieved from https://www.ngu.no/upload/Publikasjoner/Kart/B50/galdhopiggen.pdf.
Magnin, F., Etzelmüller, B., Westermann, S., Isaksen, K., Hilger, P., Hermanns, R.L., 2019. Permafrost distribution in steep rock slopes in Norway: measurements, statistical modelling and implications for geomorphological processes. Earth Surf Dynam 7 (4), 1019–1040. https://doi.org/10.5194/esurf-7-1019-2019.
Matsuoka, N., 1990. Mechanisms of rock breakdown by frost action: an experimental approach. Cold Reg. Sci. Technol. 17 (3), 253–270. https://doi.org/10.1016/S0165-232X(05)80005-9.
Matsuoka, N., Murton, J., 2008. Frost weathering: recent advances and future directions. Permafrost Periglac 19 (2), 195–210. https://doi.org/10.1002/ppp.620.
Matthews, J.A., Dresser, P.Q., 2008. Holocene glacier variation chronology of the Smørstabbtindan massif, Jotunheimen, southern Norway, and the recognition of century- to millennial-scale European Neoglacial events. The Holocene 18 (1), 181–201. https://doi.org/10.1177/0959683607085608.
Matthews, J.A., Nesje, A., 2023. Scandinavia. In: Periglacial Landscapes of Europe. Springer, pp. 365–426.
Matthews, J.A., Winkler, S., Wilson, P., Tomkins, M.D., Dortch, J.M., Mourne, R.W., Hill, J.L., Owen, G., Vater, A.E., 2018. Small rock-slope failures conditioned by Holocene permafrost degradation: a new approach and conceptual model based on Schmidt-hammer exposure-age dating, Jotunheimen, southern Norway. Boreas 47 (4), 1144–1169. https://doi.org/10.1111/bor.12336.
McCarroll, D., Shakesby, R.A., Matthews, J.A., 2001. Enhanced rockfall activity during the Little Ice Age: further lichenometric evidence from a Norwegian talus. Permafrost Periglac 12 (2), 157–164. https://doi.org/10.1002/ppp.359.
McGreevy, J.P., Whalley, W.B., 1982. The geomorphic significance of rock temperature variations in cold environments: a discussion. Arct. Alp. Res. 14 (2), 157–162. https://doi.org/10.2307/1551114.
Messenzehl, K., Meyer, H., Otto, J.-C., Hoffmann, T., Dikau, R., 2017. Regional-scale controls on the spatial activity of rockfalls (Turtmann Valley, Swiss Alps) — A multivariate modeling approach. Geomorphology 287, 29–45. https://doi.org/10.1016/j.geomorph.2016.01.008.
Murton, J.B., Peterson, R., Ozouf, J.-C., 2006. Bedrock fracture by ice segregation in cold regions. Science 314 (5802), 1127–1129. https://doi.org/10.1126/science.1132127.
Myhra, K.S., Westermann, S., Etzelmüller, B., 2017. Modelled distribution and temporal evolution of permafrost in steep rock walls along a latitudinal transect in Norway by CryoGrid 2D. Permafrost Periglac 28 (1), 172–182. https://doi.org/10.1002/ppp.1884.
Myhra, K.S., Westermann, S., Etzelmüller, B., 2019. Modeling conductive heat flow between steep rock walls and talus slopes–thermal processes and geomorphological implications. *Frontiers*. Earth Sci. 7 (192) https://doi.org/10.3389/feart.2019.00192.
Nesje, A., 2002. A large rockfall avalanche in Oldedalen, inner Nordfiord, western Norway, dated by means of a sub-avalanche Salix sp. tree trunk. Norwegian Journal of Geology/Norsk Geologisk Forening 82 (1), 59–62.
Nesje, A., 2009. Latest Pleistocene and Holocene alpine glacier fluctuations in Scandinavia. Quaternary Science Reviews 28 (21), 2119–2136. https://doi.org/10.1016/j.quascirev.2008.12.016.
Nesje, A., Blikra, L.H., Anda, E., 1994. Dating rockfall-avalanche deposits from degree of rock-surface weathering by Schmidt-hammer tests: a study from Norangsdalen, Sunnmøre. Norway. Norsk Geologisk Tidsskrift 74 (2), 108–113.
Nesje, A., Bakke, J., Dahl, S.O., Lie, Ø., Matthews, J.A., 2008. Norwegian mountain glaciers in the past, present and future. Global Planet. Change 60 (1), 10–27. https://doi.org/10.1016/j.gloplacha.2006.08.004.
Nilsen, B., Thidemann, A., 1993. Rock engineering. Norwegian Institute of Technology, Department of Hydraulic Engineering.
Noetzli, J., Gruber, S., 2009. Transient thermal effects in Alpine permafrost. The Cryosphere 3 (1), 85–99. https://doi.org/10.5194/tc-3-85-2009.
Noetzli, J., Gruber, S., Kohl, T., Salzmann, N., Haeberli, W., 2007. Three-dimensional distribution and evolution of permafrost temperatures in idealized high-mountain topography. J Geophys Res-Earth 112 (F2). https://doi.org/10.1029/2006jf000545.
North Greenland Ice Core Project Members (NGRIP), 2004. North Greenland Ice Core Project Oxygen Isotope Data. In: IGBP PAGES/World. Data Center for Paleoclimatology, Data Contribution Series # 2004–059. NOAA/NGDC Paleoclimatology Program, Boulder CO, USA.
Ødegård, R., Etzelmüller, B., Vatne, G., Sollid, J., 1995. Near-surface spring temperatures in an Arctic coastal cliff: Possible implications of rock breakdown. In: Slaymaker, O. (Ed.), Steepland Geomorphology. John Wiley & Sons, pp. 89–102.
Ødegård, R.S., Sollid, J.L., 1993. Coastal cliff temperatures related to the potential for cryogenic weathering processes, western Spitsbergen. Svalbard. Polar Research 12 (1), 95–106. https://doi.org/10.3402/polar.v12i1.6705.
Ødegård, R.S., Sollid, J.L., Liestøl, O., 1992. Ground temperature measurements in mountain permafrost, Jotunheimen, southern Norway. Permafrost Periglac 3 (3), 231–234. https://doi.org/10.1002/ppp.3430030310.
Oskin, M., Burbank, D.W., 2005. Alpine landscape evolution dominated by cirque retreat. Geology 33 (12), 933–936. https://doi.org/10.1130/g21957.1.
Paterson, W.S.B., 1994. 12 - Flow of ice shelves and ice streams. In: Paterson, W.S.B. (Ed.), The Physics of Glaciers, Third edition. Pergamon, pp. 289–316. https://doi.org/10.1016/B978-0-08-037944-9.50018-2.
Patton, H., Hubbard, A., Andreassen, K., Auriac, A., Whitehouse, P.L., Stroeven, A.P., Shackleton, C., Winsborrow, M., Heyman, J., Hall, A.M., 2017. Deglaciation of the Eurasian ice sheet complex. Quat. Sci. Rev. 169, 148–172. https://doi.org/10.1016/j.quascirev.2017.05.019.
Prabhakaran, R., Bruna, P.O., Bertotti, G., Smeulders, D., 2019. An automated fracture trace detection technique using the complex shearlet transform. Solid Earth 10 (6), 2137–2166. https://doi.org/10.5194/se-10-2137-2019.
Rapp, A., 1960. Recent development of mountain slopes in Karkevagge and Surroundings, Northern Scandinavia. Geografiska Annaler 42 (2/3), 65–200. https://doi.org/10.2307/520126.
Ravanel, L., Deline, P., 2011. Climate influence on rockfalls in high-Alpine steep rockwalls: the north side of the Aiguilles de Chamonix (Mont Blanc massif) since the end of the 'Little Ice Age'. Holocene 21 (2), 357–365. https://doi.org/10.1177/0959683610374887.
Rempel, A.W., Van Alst, L.J., 2013. Potential gradients produced by pore-space heterogeneities: application to isothermal frost damage and submarine hydrate anomalies. In: Poromechanics V Proceedings of the Fifth Biot Conference on Poromechanics, pp. 813–822. https://doi.org/10.1061/9780784412992.098.
Rempel, A.W., Marshall, J.A., Roering, J.J., 2016. Modeling relative frost weathering rates at geomorphic scales. Earth Planet. Sci. Lett. 453, 87–95. https://doi.org/10.1016/j.epsl.2016.08.019.
Sanders, J.W., Cuffey, K.M., Moore, J.R., MacGregor, K.R., Kavanaugh, J.L., 2012. Periglacial weathering and headwall erosion in cirque glacier bergschrunds. Geology 40 (9), 779–782. https://doi.org/10.1130/g33330.1.
Sandersen, F., Bakkehøi, S., Hestnes, E., Lied, K., 1997. The influence of meteorological factors on the initiation of debris flows, rockfalls, rockslides and rockmass stability. Norges Geotekniske Institutt 201, 97–114.
Sass, O., 2005a. Rock moisture measurements: techniques, results, and implications for weathering. Earth Surf Proc Land 30 (3), 359–374. https://doi.org/10.1002/esp.1214.
Sass, O., 2005b. Temporal Variability of Rockfall in the Bavarian Alps, Germany. Arct. Antarct. Alp. Res. 37 (4), 564–573. https://doi.org/10.1657/1523-0430(2005)037[0564:TVORIT]2.0.CO;2.
Savi, S., Delunel, R., Schlunegger, F., 2015. Efficiency of frost-cracking processes through space and time: an example from the eastern Italian Alps. Geomorphology 232, 248–260. https://doi.org/10.1016/j.geomorph.2015.01.009.
Smith, M.W., Riseborough, D.W., 2002. Climate and the limits of permafrost: a zonal analysis. Permafrost Periglac 13 (1), 1–15. https://doi.org/10.1002/ppp.410.
Steer, P., Huismans, R.S., Valla, P.G., Gac, S., Herman, F., 2012. Bimodal Plio–Quaternary glacial erosion of fjords and low-relief surfaces in Scandinavia. Nat. Geosci. 5 (9), 635–639. https://doi.org/10.1038/ngeo1549.
Støren, E.N., Dahl, S.O., Lie, Ø., 2008. Separation of late-Holocene episodic paraglacial events and glacier fluctuations in eastern Jotunheimen, central southern Norway. The Holocene 18 (8), 1179–1191. https://doi.org/10.1177/0959683608096593.
Stroeven, A.P., Hättestrand, C., Kleman, J., Heyman, J., Fabel, D., Fredin, O., Goodfellow, B.W., Harbor, J.M., Jansen, J.D., Olsen, L., Caffee, M.W., Fink, D., Lundqvist, J., Rosqvist, G.C., Strömberg, B., Jansson, K.N., 2016. Deglaciation of Fennoscandia. Quaternary Science Reviews 147, 91–121. https://doi.org/10.1016/j.quascirev.2015.09.016.
Stuart-Smith, R.F., Roe, G.H., Li, S., Allen, M.R., 2021. Increased outburst flood hazard from Lake Palcacocha due to human-induced climate change. Nat. Geosci. 14, 85–90. https://doi.org/10.1038/s41561-021-00686-4.
Vie, E.H., 2012. *Kvartærgeologisk kartlegging og rekonstruksjon av isavsmeltinga i Grødalen, Sunndalsfjella* [MSc thesis, University of Bergen].
Vlahou, I., Worster, M.G., 2010. Ice growth in a spherical cavity of a porous medium. J. Glaciol. 56 (196), 271–277. https://doi.org/10.3189/002214310791968494.
Walder, J., Hallet, B., 1985. A theoretical model of the fracture of rock during freezing. GSA Bull. 96 (3), 336–346. https://doi.org/10.1130/0016-7606(1985)96<336:ATMOTF>2.0.CO;2.
Walder, J.S., Hallet, B., 1986. The physical basis of frost weathering: toward a more fundamental and unified perspective. Arctic and Alpine Research 18 (1), 27–32. https://doi.org/10.2307/1551211.